

Modeling ternary fluids in contact with elastic membranes

M. Pepona ¹, A. C. M. Shek,¹ C. Semperebon ², T. Krüger ³, and H. Kusumaatmaja ^{1,*}

¹*Department of Physics, Durham University, South Road, Durham DH1 3LE, United Kingdom*

²*Smart Materials and Surfaces Laboratory, Department of Mathematics, Physics and Electrical Engineering, Ellison Place, Northumbria University, Newcastle upon Tyne, NE1 8ST, United Kingdom*

³*School of Engineering, Institute for Multiscale Thermo fluids, The University of Edinburgh, Edinburgh EH9 3FB, Scotland, United Kingdom*



(Received 20 May 2020; revised 2 December 2020; accepted 15 January 2021; published 8 February 2021)

We present a thermodynamically consistent model of a ternary fluid interacting with elastic membranes. Following a free-energy modeling approach for the fluid phases, we derive the governing equations for the dynamics of the ternary fluid flow and membranes. We also provide the numerical framework for simulating such fluid-structure interaction problems. It is based on the lattice Boltzmann method for the ternary fluid (Eulerian description) and a finite difference representation of the membrane (Lagrangian description). The ternary fluid and membrane solvers are coupled through the immersed boundary method. For validation purposes, we consider the relaxation dynamics of a two-dimensional elastic capsule placed at a fluid-fluid interface. The capsule shapes, resulting from the balance of surface tension and elastic forces, are compared with equilibrium numerical solutions obtained by SURFACE EVOLVER. Furthermore, the Galilean invariance of the proposed model is proven. The proposed approach is versatile, allowing for the simulation of a wide range of geometries. To demonstrate this, we address the problem of a capillary bridge formed between two deformable capsules.

DOI: [10.1103/PhysRevE.103.022112](https://doi.org/10.1103/PhysRevE.103.022112)

I. INTRODUCTION

Multiphase and multicomponent flows in interaction with deformable, thin structures are encountered in a broad range of applications. One example of such flows are capsules accommodating multiple aqueous solutions, such as polyethylene glycol and dextran, serving as model biological cells [1,2]. Artificially fabricated elastic capsules [3] are also employed as container and delivery systems in many industrial applications, for instance, in drug delivery [4] and various processes in the cosmetic [5] and food [6] industries. Another case where a multicomponent flow interacting with soft particles occurs is in the self-assembly of colloidal aggregates into patchy particles, a phenomenon of particular importance for the successful design of bottom-up materials [7,8]. These patchy particles can be formed of compartments, each containing different polymers, bonded together by a solvent. The wetting of liquid droplets surrounded by air on soft solids is another example of multiphase flows in contact with deformable structures, with relevance in biology, e.g., cell locomotion [9], medicine and engineering, e.g., in the identification of cancer cells [10], and in the development of smart coatings [11]. Similar elastocapillary problems also arise with fibrous materials, such as the coalescence of wet hair [12].

Even though these elastocapillary problems have been extensively studied both analytically and experimentally [13–26], the accurate computational modeling of such configurations is lagging behind. Elastic liquid-core capsules,

obeying various constitutive laws, immersed in another fluid component constitute the most widely studied computational configuration [27–34]. A comprehensive review on such configuration is given by Barthès-Biesel [35]. All these computational works have not dealt with the contact line problem that arises when two or more fluids are in contact with the same side of a membrane. With respect to elastocapillary problems involving contact lines, there has been an attempt by Lubbers *et al.* [36] to numerically solve the equilibrium shape problem of liquid droplets on soft solids. The equilibrium shapes are obtained by minimizing the total elastocapillary energy of the vapor-liquid-substrate system; thus, no fluid dynamics properties of the droplets and surrounding air are available. Only recently, methods capable of capturing contact line dynamics have started to be developed. For instance, Bueno *et al.* [37] proposed a numerical framework for the simulation of binary fluids in contact with nonlinear hyperelastic solids to investigate the wetting of soft substrates and elastic micropillars. Wouters *et al.* [38] developed a numerical framework allowing for the simulation of soft particles at fluid-fluid interfaces.

The aim of this work is to analytically derive a thermodynamically consistent model of multicomponent fluids in interaction with elastic membranes, and to provide a versatile numerical framework for the simulation of such fluid-structure interaction problems. We focus here on the case of a ternary fluid where one component is enclosed inside the membranes. The model can, however, be generalized to consider more fluid components contained in or surrounding the membranes. The availability of such computational method will allow us to systematically study a wide range of elastocapillary phenomena intractable to analytical solutions,

*halim.kusumaatmaja@durham.ac.uk

in order to complement expanding experimental activities in this area.

We follow a top-down modeling approach for the ternary fluid using the lattice Boltzmann method [39–46]; namely, the free energy of the fluid system is initially formulated, including the desired thermodynamics features. Given the free energy, the macroscopic equations of motion of the multicomponent fluid can be derived. This technique is the contrary of the bottom-up modeling approach, where the macroscopic properties of the fluid arise from the microscopic interactions between the fluid particles, with these interactions usually taking the form of an interparticle potential [47,48]. Krüger *et al.* [49] have discussed in detail the advantages and limitations of each of these modeling approaches. The lattice Boltzmann model proposed by Semperebon *et al.* [45] has been in particular chosen here for resolving the flow in a uniform, Cartesian grid. This is a diffuse interface model, meaning that the fluid-fluid interfaces are spread over several lattices, rather than being tracked explicitly. The capsules enclosing one fluid component are modeled here as infinitely thin membranes, composed of a homogeneous and isotropic material, able to undergo stretching or compression and bending. To resolve the interaction between the ternary fluid and the membranes, we adopt the immersed boundary method (IBM), initially proposed by Peskin [50]. This allows for solving the equations of motion of the ternary fluid in an Eulerian description, while the membranes' ones are solved in a Lagrangian coordinate system, following the motion and deformation of the membrane's boundary.

The article is organized as follows. In Sec. II, we present a thermodynamically consistent model of a ternary fluid in contact with elastic membranes. The methods employed here for the numerical solution of the ternary fluid and its interacting membranes equations of motion are subsequently presented in Secs. III A–III C. The SURFACE EVOLVER [51], an open-source software used for benchmarking purposes, is briefly discussed in Sec. III D. We then validate our model against SURFACE EVOLVER in Sec. IV A, considering a two-dimensional elastic capsule placed at a fluid-fluid interface as the benchmark configuration. We also prove the Galilean invariance of the equations governing the ternary fluid flow and the membranes' dynamics. To demonstrate the versatility of our model, the problem of a capillary bridge formed between two elastic capsules is afterwards studied in Sec. IV B. For simplicity, here we focus on two dimensions. Finally, the key contributions of this work and its future perspectives are summarized in Sec. V.

II. MATHEMATICAL MODELING OF TERNARY FLUIDS IN INTERACTION WITH ELASTIC MEMBRANES

In this section, we first present briefly the free energy of the ternary fluid, which is based on the one proposed by Semperebon *et al.* [45] but modified accordingly in order to account for the interplay between the fluid and the membrane. We subsequently formulate the strain and bending energies of the elastic membrane. Finally, the equations of motion for the ternary fluid interacting with elastic membranes are introduced.

To clarify notations, bold lowercase letters are employed for vector variables evaluated on the Eulerian lattices, while bold uppercase ones refer to vector variables defined at the Lagrangian markers.

A. Free energy of the ternary fluid

In this article, we are concerned with cases in which there are three fluid components, and without any loss of generality, we will assume that the fluid component 3 is enclosed inside the membrane. The free energy F_f of the ternary fluid system considered here is the sum of two contributions: a Landau free-energy functional \mathcal{E}_f allowing the coexistence of three fluid components, and a coupling-energy functional \mathcal{E}_c taking into account the interaction between the membrane and its confined fluid component

$$F_f = \mathcal{E}_f + \mathcal{E}_c. \quad (1)$$

In this work, we use the following forms for \mathcal{E}_f and \mathcal{E}_c :

$$\begin{aligned} \mathcal{E}_f &= \int_V [f_{b,f} + f_{\nabla}] dV \\ &= c_s^2 \rho \ln \rho + \sum_{m=1}^{N=3} \int_V \left[\frac{\kappa_m}{2} C_m^2 (1 - C_m)^2 \right. \\ &\quad \left. + \frac{\alpha^2 \kappa_m}{2} (\nabla C_m)^2 \right] dV, \end{aligned} \quad (2)$$

$$\mathcal{E}_c = \int_V f_{b,c} dV = \int_V \frac{\kappa_c}{2} (C_3 - \mathcal{I})^2 dV, \quad (3)$$

where C_m represents the density of the fluid component m ($m = 1, 2, 3$), $\rho = \sum_m C_m$ is the total mass density, c_s denotes the speed of sound, κ_m are tunable parameters related to the fluid surface tensions, κ_c denotes the coupling coefficient, and the integration takes place over the simulation volume V . The free-energy density of the bulk fluid mixture $f_{b,f}$ is composed of the first two terms on the right-hand side of Eq. (2), while the interfacial free-energy density f_{∇} comprises the last term. The same form for \mathcal{E}_f is considered in the ternary fluid model proposed by Semperebon *et al.* [45], whereas the aforementioned model differs from the present one in that no coupling-energy functional $f_{b,c}$ [Eq. (3)] is taken into consideration. \mathcal{I} is an interfacial profile that we construct from the membrane, as described below in Eq. (7).

Following the form of the bulk free-energy density $f_{b,f}$, each fluid density C_m has two bulk minima at $C_m = \{0, 1\}$, where we drop the physical units in the following for brevity. For the ternary fluid system of interest, only the following three minimizers are relevant:

$$\begin{aligned} C_1 = 1, \quad C_2 = 0, \quad C_3 = 0; \\ C_1 = 0, \quad C_2 = 1, \quad C_3 = 0; \\ C_1 = 0, \quad C_2 = 0, \quad C_3 = 1, \end{aligned} \quad (4)$$

corresponding to the three bulk fluids in the ternary system. Our multicomponent fluid model is a diffuse interface model; when the fluid transitions from one bulk component to another, the interfacial profile assumes the form

$$C_m = \frac{1 + \tanh [d_{FI}/(2\alpha)]}{2}, \quad (5)$$

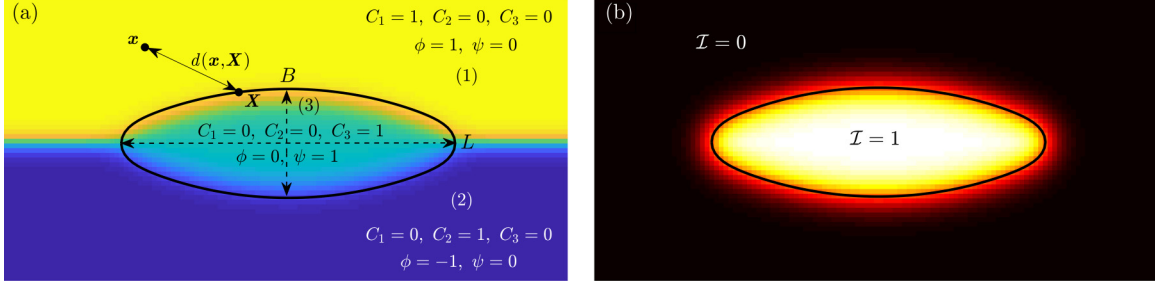


FIG. 1. (a) Representative schematic diagram of an elastic membrane (solid lines), enclosing the fluid component (3), suspended at the interface between fluids (1) and (2). \mathbf{x} and \mathbf{X} denote, respectively, the positions of a fluid and membrane point, with $d(\mathbf{x}, \mathbf{X})$ the distance between them. (b) A sample interfacial profile \mathcal{I} field across the elastic membrane.

where d_{FI} measures the distance between the bulk fluid at position \mathbf{x} and the fluid-fluid interface. Equation (5) ensures that $C_m \rightarrow 1$ for $d_{\text{FI}} \rightarrow \infty$, and $C_m \rightarrow 0$ for $d_{\text{FI}} \rightarrow -\infty$. The parameter α is proportional to the interface width, which here is chosen the same for all three fluid-fluid interfaces. The fluid-fluid surface tensions are expressed as

$$\gamma_{mn} = \frac{\alpha}{6}(\kappa_m + \kappa_n), \quad m, n = 1, 2, 3 \text{ and } m \neq n. \quad (6)$$

The coupling energy is formulated in such a way that for $\kappa_c > 0$ there is a minimum when $C_3 = \mathcal{I}$. The interfacial profile \mathcal{I} across the elastic membrane is then defined as

$$\mathcal{I} = \frac{1 + \tanh[d(\mathbf{x}, \mathbf{X})/(2\alpha)]}{2}, \quad (7)$$

where $d(\mathbf{x}, \mathbf{X})$ denotes the distance between the fluid at position \mathbf{x} and the membrane located at \mathbf{X} , as shown in Fig. 1(a). This distance is assigned to be positive for the enclosed fluid component 3, and negative for the surrounding fluid components 1 and 2. The width of the fluid-membrane interfaces is kept the same as the fluid-fluid interfaces one by assigning the same value to the parameter α in Eqs. (5) and (7). Similarly to C_m , $\mathcal{I} \rightarrow 1$ for $d(\mathbf{x}, \mathbf{X}) \rightarrow \infty$, and $\mathcal{I} \rightarrow 0$ for $d(\mathbf{x}, \mathbf{X}) \rightarrow -\infty$, as depicted in Fig. 1(b). It should be noted that changes in the free-energy functional will reflect on the definition of \mathcal{I} . It is obvious that with an increasing coupling coefficient κ_c , the interfacial profile for the density C_3 of the enclosed fluid component will be superimposed onto the profile of the fluid 3-membrane interface. However, if κ_c is too high, the coupling-energy term will dominate over the rest of the free-energy terms, which is undesirable and may even lead to numerical instabilities.

B. Strain and bending energies of the elastic membrane

The formulations of \mathcal{E}_s and \mathcal{E}_b depend on the nature of the membrane material. Here, we consider the simple case of a linear elastic material, for which the strain energy takes the form of Hooke's law, and the bending energy is given by the squared mean curvature. However, the strain and bending energy formulations can be modified to model more realistic materials. Thus, the strain and bending energies are expressed as

$$\mathcal{E}_s = \int_S \frac{\kappa_s}{2} \left(\left| \frac{\partial \mathbf{X}}{\partial \mathbf{s}} \right| - 1 \right)^2 ds \quad (8)$$

and

$$\mathcal{E}_b = \int_S \frac{\kappa_b}{2} \left(\frac{\partial \theta}{\partial s'} \right)^2 ds. \quad (9)$$

The integration takes place over the surface S of the elastic membrane, whose position in Eulerian coordinates at time t is described by $\mathbf{X} = \mathbf{X}(s, t)$, with s denoting its undeformed Lagrangian coordinates. The parameters κ_s and κ_b are, respectively, the stretching and bending moduli. $\partial \theta / \partial s'$ denotes the membrane curvature, which depends on how the tangential angle $\theta = \theta(\mathbf{X})$ varies across the deformed membrane surface, described by $s' = s'(\mathbf{X})$.

C. Equations of motion

Following the rationale of Kou and Sun [52], we derive the equations of motion for the fluids and the elastic membrane, making use of the first and second laws of thermodynamics. The complete derivation is provided in the Appendix. For convenience, we will also introduce the total mass density ρ , and two auxiliary fields ϕ and ψ , given by

$$\rho = C_1 + C_2 + C_3, \quad \phi = C_1 - C_2, \quad \psi = C_3. \quad (10)$$

Here, we assume that all fluid components have the same density, and thus the total mass density is set to be $\rho = 1$.

Using ρ , ϕ , and ψ , the equations of motion for the fluid components are given by the continuity, Navier-Stokes, and two Cahn-Hilliard equations

$$\frac{\partial \rho}{\partial t} + \nabla \cdot (\rho \mathbf{u}) = 0, \quad (11)$$

$$\begin{aligned} \frac{\partial (\rho \mathbf{u})}{\partial t} + \nabla \cdot (\rho \mathbf{u} \otimes \mathbf{u}) = & -\nabla p_i + \nabla \cdot [\eta(\nabla \mathbf{u} + \nabla \mathbf{u}^T)] \\ & - \rho \nabla \mu_\rho - \phi \nabla \mu_\phi - \psi \nabla \mu_\psi \\ & - \psi \nabla \left(\frac{\delta f_{b,c}}{\delta \psi} \right), \end{aligned} \quad (12)$$

$$\frac{\partial \phi}{\partial t} + \nabla \cdot (\phi \mathbf{u}) = M_\phi \nabla^2 \mu_\phi, \quad (13)$$

$$\frac{\partial \psi}{\partial t} + \nabla \cdot (\psi \mathbf{u}) = M_\psi \nabla^2 \mu'_\psi = M_\psi \nabla^2 \left(\mu_\psi + \frac{\delta f_{b,c}}{\delta \psi} \right), \quad (14)$$

where \mathbf{u} , $p_i = \rho c_s^2$, η , M_ϕ , and M_ψ are, respectively, the mass-averaged velocity, the ideal gas pressure, the fluid dynamic viscosity, and the two mobility parameters in the

Cahn-Hilliard equations. We assume that all fluid components C_m ($m = 1, 2, 3$) have identical mobility parameters, resulting in $M_\phi = 3M_\psi$ when the auxiliary variables are employed. μ_ρ , μ_ϕ , and μ_ψ are the chemical potentials coming from the chosen free-energy density of the ternary fluid. The detailed formulations of the chemical potentials μ_ρ , μ_ϕ , and μ_ψ in terms of the variables ρ , ϕ , and ψ are given by

$$\begin{aligned} \mu_\rho = & \frac{\kappa_1}{8}(\rho + \phi - \psi)(\rho + \phi - \psi - 1)(\rho + \phi - \psi - 2) \\ & + \frac{\kappa_2}{8}(\rho - \phi - \psi)(\rho - \phi - \psi - 1)(\rho - \phi - \psi - 2) \\ & + \frac{\alpha^2}{4}[(\kappa_1 + \kappa_2)(\nabla^2\psi - \nabla^2\rho) + (\kappa_2 - \kappa_1)\nabla^2\phi], \end{aligned} \quad (15)$$

$$\begin{aligned} \mu_\phi = & \frac{\kappa_1}{8}(\rho + \phi - \psi)(\rho + \phi - \psi - 1)(\rho + \phi - \psi - 2) \\ & - \frac{\kappa_2}{8}(\rho - \phi - \psi)(\rho - \phi - \psi - 1)(\rho - \phi - \psi - 2) \\ & + \frac{\alpha^2}{4}[(\kappa_2 - \kappa_1)(\nabla^2\rho - \nabla^2\psi) - (\kappa_1 + \kappa_2)\nabla^2\phi], \end{aligned} \quad (16)$$

$$\begin{aligned} \mu_\psi = & -\frac{\kappa_1}{8}(\rho + \phi - \psi)(\rho + \phi - \psi - 1)(\rho + \phi - \psi - 2) \\ & - \frac{\kappa_2}{8}(\rho - \phi - \psi)(\rho - \phi - \psi - 1)(\rho - \phi - \psi - 2) \\ & + \frac{\alpha^2}{4}[(\kappa_1 + \kappa_2)\nabla^2\rho - (\kappa_2 - \kappa_1)\nabla^2\phi \\ & - (\kappa_1 + \kappa_2 + 4\kappa_3)\nabla^2\psi] + \kappa_3\psi(\psi - 1)(2\psi - 1). \end{aligned} \quad (17)$$

It readily follows from Eq. (3) that $\delta f_{b,c}/\delta\psi = \kappa_c(\psi - \mathcal{I})$.

To be consistent with the work of Sempregon *et al.* [45], the ideal gas pressure p_i is written as a separate term in the Navier-Stokes equation (12) instead of being included into the definition of μ_ρ , Eq. (15). Since the total mass density is set to $\rho = 1$ everywhere in this work, the chemical potential term μ_ρ is essentially a constant and it does not play any significant role in the Navier-Stokes equation. Compared to previous ternary free-energy lattice Boltzmann models, such as by Sempregon *et al.* [45], the present model is differentiated by the last term on the right-hand side of Eq. (12) and the additional term $\delta f_{b,c}/\delta\psi$ in the chemical potential μ'_ψ , Eq. (14). Both terms are due to the coupling-energy functional between the fluid and the membrane. As we will discuss in Sec. III, another key difference to previously published models is the use of immersed boundary method to couple the fluid and membrane dynamics.

The membrane is discretized by a collection of Lagrangian markers. The variable \mathbf{X}_l denotes the position of the l th Lagrangian marker (in Eulerian coordinates), with $l = 1, \dots, N_l$. The equation of motion for each Lagrangian marker is given by

$$m \frac{d^2 \mathbf{X}_l}{dt^2} = \mathbf{F}_{\text{mem},l} = \mathbf{F}_{s,l} + \mathbf{F}_{b,l} + \mathbf{F}_{c,l}, \quad (18)$$

where \mathbf{F}_{mem} denotes the total force exerted on the elastic membrane, and

$$\mathbf{F}_{s,l} = -\frac{\partial \mathcal{E}_s}{\partial \mathbf{X}_l}, \quad \mathbf{F}_{b,l} = -\frac{\partial \mathcal{E}_b}{\partial \mathbf{X}_l}, \quad \mathbf{F}_{c,l} = -\frac{\partial \mathcal{E}_c}{\partial \mathbf{X}_l} \quad (19)$$

are the strain, bending, and coupling forces, respectively. The detailed forms of $\mathbf{F}_{s,l}$, $\mathbf{F}_{b,l}$, and $\mathbf{F}_{c,l}$ are provided in Sec. III B.

III. NUMERICAL METHODS

In this section, the numerical techniques employed for the solution of the equations of motion of the ternary fluid and its interacting elastic membrane are discussed. The governing equations of the ternary fluid are solved numerically by means of a lattice Boltzmann method, as detailed in Sec. III A. The discretized forms of the strain, bending, and coupling energies are presented in Sec. III B along with the corresponding force formulations. The interaction between the ternary fluid and elastic membrane is solved by an immersed boundary method, described in Sec. III C, that is coupled to the lattice Boltzmann method following the algorithm presented in Krüger *et al.* [53]. Finally, we briefly report the equivalent energy implementation in SURFACE EVOLVER, a finite element approach employed to benchmark the equilibrium solutions of wetting elastic membranes, in Sec. III D.

A. Lattice Boltzmann method

To solve the equations of motion of the ternary fluid, Eqs. (11)–(14), we employ the lattice Boltzmann method with three sets of distribution functions $f_i(\mathbf{x}, t)$, $g_i(\mathbf{x}, t)$, and $h_i(\mathbf{x}, t)$, corresponding to the total fluid density ρ and the auxiliary fields ϕ and ψ . The evolutions of the distribution functions are governed by the lattice Boltzmann equation, where the standard Bhatnagar-Gross-Krook (BGK) single relaxation time model [54] is used for the collision operator, and the exact difference scheme [55] is employed for the forcing term

$$\begin{aligned} f_i(\mathbf{x} + \mathbf{c}_i \Delta t, t + \Delta t) = & f_i(\mathbf{x}, t) - \frac{\Delta t}{\tau} [f_i(\mathbf{x}, t) - f_i^{\text{eq}}(\rho, \mathbf{u})] \\ & + \Delta t [f_i^{\text{eq}}(\rho, \mathbf{u} + \delta \mathbf{u}) - f_i^{\text{eq}}(\rho, \mathbf{u})], \\ g_i(\mathbf{x} + \mathbf{c}_i \Delta t, t + \Delta t) = & g_i(\mathbf{x}, t) - \frac{\Delta t}{\tau_\phi} [g_i(\mathbf{x}, t) - g_i^{\text{eq}}(\phi, \mathbf{v})], \\ h_i(\mathbf{x} + \mathbf{c}_i \Delta t, t + \Delta t) = & h_i(\mathbf{x}, t) - \frac{\Delta t}{\tau_\psi} [h_i(\mathbf{x}, t) - h_i^{\text{eq}}(\psi, \mathbf{v})]. \end{aligned} \quad (20)$$

The variables $f_i(\mathbf{x}, t)$, $g_i(\mathbf{x}, t)$, and $h_i(\mathbf{x}, t)$ refer to the distribution functions f_i , g_i , and h_i at position \mathbf{x} and time t with velocity \mathbf{c}_i along the i th lattice direction. The relaxation times τ , τ_ϕ , and τ_ψ are linked to the dynamic viscosity η , and the mobility parameters M_ϕ and M_ψ by

$$\begin{aligned} \eta = & \rho c_s^2 \left(\tau - \frac{\Delta t}{2} \right), \\ M_\phi = & \Gamma_\phi \left(\tau_\phi - \frac{\Delta t}{2} \right), \\ M_\psi = & \Gamma_\psi \left(\tau_\psi - \frac{\Delta t}{2} \right), \end{aligned} \quad (21)$$

where c_s is the speed of sound, and Γ_ϕ , Γ_ψ are tunable parameters. The speed of sound is given by $c_s = \frac{1}{\sqrt{3}}c$, where $c = \frac{\Delta x}{\Delta t}$

is the lattice speed, and Δx , Δt are the lattice spacing and time step, respectively. The variables f_i^{eq} , g_i^{eq} , and h_i^{eq} denote the equilibrium distribution functions.

The equilibrium distribution functions are expressed as

$$\begin{aligned} f_i^{\text{eq}}(\rho, \mathbf{u}) &= w_i \rho \left[1 + \frac{\mathbf{c}_i \cdot \mathbf{u}}{c_s^2} + \frac{\mathbf{u} \mathbf{u} : (\mathbf{c}_i \mathbf{c}_i - c_s^2 \mathbf{I})}{2c_s^4} \right], \\ g_i^{\text{eq}}(\phi, \mathbf{v}) &= \begin{cases} w_i \left[\frac{\Gamma_\phi \mu_\phi}{c_s^2} + \frac{\phi \mathbf{c}_i \cdot \mathbf{v}}{c_s^2} + \frac{\phi \mathbf{v} \mathbf{v} : (\mathbf{c}_i \mathbf{c}_i - c_s^2 \mathbf{I})}{2c_s^4} \right], & i \neq 0 \\ \phi - \sum_{i, i \neq 0} g_i^{\text{eq}}, & i = 0 \end{cases} \\ h_i^{\text{eq}}(\psi, \mathbf{v}) &= \begin{cases} w_i \left[\frac{\Gamma_\psi \mu'_\psi}{c_s^2} + \frac{\psi \mathbf{c}_i \cdot \mathbf{v}}{c_s^2} + \frac{\psi \mathbf{v} \mathbf{v} : (\mathbf{c}_i \mathbf{c}_i - c_s^2 \mathbf{I})}{2c_s^4} \right], & i \neq 0 \\ \psi - \sum_{i, i \neq 0} h_i^{\text{eq}}, & i = 0 \end{cases} \end{aligned} \quad (22)$$

where w_i are weight coefficients depending on the chosen lattice arrangement for the velocity discretization, and \mathbf{I} is the identity tensor.

The macroscopic physical variables are defined as moments of the distribution functions

$$\begin{aligned} \rho(\mathbf{x}, t) &= \sum_i f_i(\mathbf{x}, t), \\ \mathbf{u}(\mathbf{x}, t) &= \left(\sum_i \mathbf{c}_i f_i(\mathbf{x}, t) \right) / \rho(\mathbf{x}, t), \\ \phi(\mathbf{x}, t) &= \sum_i g_i(\mathbf{x}, t), \\ \psi(\mathbf{x}, t) &= \sum_i h_i(\mathbf{x}, t). \end{aligned} \quad (23)$$

The densities C_m can then be reconstructed by using the inverse variables transformation of Eq. (10):

$$C_1 = (\rho + \phi - \psi)/2, \quad C_2 = (\rho - \phi - \psi)/2, \quad C_3 = \psi. \quad (24)$$

The variable \mathbf{u} represents the bare fluid velocity, and it is related to the actual fluid velocity \mathbf{v} by

$$\mathbf{v}(\mathbf{x}, t) = \mathbf{u}(\mathbf{x}, t) + \delta \mathbf{u}(\mathbf{x}, t)/2, \quad (25)$$

where $\delta \mathbf{u}$ denotes the velocity correction given by

$$\delta \mathbf{u}(\mathbf{x}, t) = \frac{\mathbf{f}(\mathbf{x}, t)}{\rho(\mathbf{x}, t)} \Delta t. \quad (26)$$

The forcing term \mathbf{f} can be considered as the sum of three contributions: a force \mathbf{f}_{FE} taking into account the gradient terms on the right-hand side of Eq. (12), a force \mathbf{f}_{IB} accounting for the interaction between the ternary fluid and elastic membrane, and a force \mathbf{f}_{ext} allowing the existence of external forces

$$\mathbf{f} = \mathbf{f}_{\text{FE}} + \mathbf{f}_{\text{IB}} + \mathbf{f}_{\text{ext}}. \quad (27)$$

The force \mathbf{f}_{FE} can be written as

$$\mathbf{f}_{\text{FE}} = -\rho \nabla \mu_\rho - \phi \nabla \mu_\phi - \psi \nabla \mu_\psi - \psi \nabla \left(\frac{\delta f_{\text{b,c}}}{\delta \psi} \right). \quad (28)$$

The form of the force \mathbf{f}_{IB} is discussed in Sec. III C. In this work, no external forces are considered, that is $\mathbf{f}_{\text{ext}} = \mathbf{0}$.

In summary, the present lattice Boltzmann model differs from the one proposed by Semperebon *et al.* [45] for ternary fluids in the following ways: (1) the added term

$\delta f_{\text{b,c}}/\delta \psi$ in the chemical potential μ'_ψ , (2) the added term $-\psi \nabla (\delta f_{\text{b,c}}/\delta \psi)$ in Eq. (28), and (3) the inclusion of the immersed boundary forces \mathbf{f}_{IB} in Eq. (27).

In lattice units, the lattice spacing and time step are for simplicity set equal to 1, $\Delta x = \Delta t = 1$, resulting in $c = 1$ and $c_s = 1/\sqrt{3}$. Here, we employ the D2Q9 lattice arrangement, for which the lattice velocities (in columns) are defined as

$$\mathbf{c}_i = c \begin{bmatrix} 0 & 1 & -1 & 0 & 0 & 1 & -1 & -1 & 1 \\ 0 & 0 & 0 & 1 & -1 & 1 & -1 & 1 & -1 \end{bmatrix},$$

and the weight coefficients are given by

$$w_0 = \frac{4}{9}, \quad w_{1-4} = \frac{1}{9}, \quad w_{5-8} = \frac{1}{36}.$$

B. Membrane dynamics

The discretized strain and bending energies of the elastic membrane, given respectively by Eqs. (8) and (9) in its continuous-space forms, are formulated as

$$\mathcal{E}_s = \frac{\kappa_s}{2} \sum_{l=1}^{N_l} \left(\frac{|\mathbf{X}_{l+1} - \mathbf{X}_l|}{\Delta s} - 1 \right)^2 \Delta s, \quad (29)$$

$$\mathcal{E}_b = \frac{\kappa_b}{2} \sum_{l=1}^{N_l} \left(\frac{\Delta \theta}{\Delta s'} \right)^2 \Delta s. \quad (30)$$

The summation occurs over all the Lagrangian markers $l = 1, \dots, N_l$. The variable \mathbf{X}_l denotes the position of the l th Lagrangian marker (in Eulerian coordinates), and Δs represents the initial distance between two consecutive Lagrangian markers. The membrane is initially discretized into Lagrangian markers such that $\Delta s = \Delta x = 1$. The tangential angle $\Delta \theta$ and arc length $\Delta s'$ of the circumscribed circle passing through the Lagrangian marker l and its neighboring points, depicted in Fig. 2, can be expressed as

$$\Delta \theta(l) = 2 \arccos \left[\frac{(\mathbf{X}_{l+1} - \mathbf{X}_l) \cdot (\mathbf{X}_l - \mathbf{X}_{l-1})}{|\mathbf{X}_{l+1} - \mathbf{X}_l| |\mathbf{X}_l - \mathbf{X}_{l-1}|} \right], \quad (31)$$

$$\Delta s'(l) = |\mathbf{X}_l - \mathbf{X}_{l-1}| + |\mathbf{X}_{l+1} - \mathbf{X}_l|. \quad (32)$$

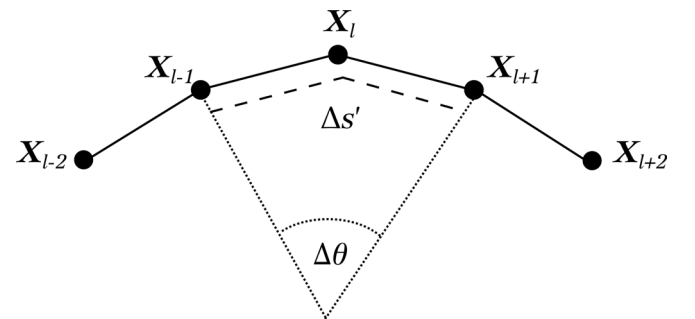


FIG. 2. The membrane (solid lines) is discretized into points (filled circles), referred to as Lagrangian markers. $\Delta \theta$ (dotted lines) and $\Delta s'$ (dashed lines) represent the tangential angle and arc length of the circumscribed circle passing through the Lagrangian marker X_l and its neighboring points X_{l-1} and X_{l+1} .

Taking into account Eqs. (29)–(32), the corresponding discretized strain and bending forces can then be found as

$$\mathbf{F}_{s,l} = -\frac{\partial \mathcal{E}_s}{\partial \mathbf{X}_l} = -\sum_{m=1}^{N_l} \kappa_s \left(\frac{|\mathbf{X}_{m+1} - \mathbf{X}_m|}{\Delta s} - 1 \right) \frac{(\mathbf{X}_{m+1} - \mathbf{X}_m)}{|\mathbf{X}_{m+1} - \mathbf{X}_m|} (\delta_{m+1,l} - \delta_{m,l}) \quad (33)$$

and

$$\mathbf{F}_{b,l} = -\frac{\partial \mathcal{E}_b}{\partial \mathbf{X}_l} = -\sum_{m=1}^{N_l} \frac{\kappa_b}{4} \left[2 \frac{\Delta \theta(m)}{\Delta s'(m)} \frac{\partial \Delta \theta(m)}{\partial \mathbf{X}_l} - \left(\frac{\Delta \theta(m)}{\Delta s'(m)} \right)^2 \frac{\partial \Delta s'(m)}{\partial \mathbf{X}_l} \right], \quad (34)$$

where

$$\begin{aligned} \frac{\partial \Delta \theta(m)}{\partial \mathbf{X}_l} &= -\frac{2}{\sqrt{1-y^2(m)}} \left[\left(\frac{(\mathbf{X}_m - \mathbf{X}_{m-1})}{|\mathbf{X}_{m+1} - \mathbf{X}_m| |\mathbf{X}_m - \mathbf{X}_{m-1}|} - \frac{(\mathbf{X}_{m+1} - \mathbf{X}_m) \cdot (\mathbf{X}_m - \mathbf{X}_{m-1})}{|\mathbf{X}_{m+1} - \mathbf{X}_m|^3 |\mathbf{X}_m - \mathbf{X}_{m-1}|} (\mathbf{X}_{m+1} - \mathbf{X}_m) \right) (\delta_{m+1,l} - \delta_{m,l}) \right. \\ &\quad \left. + \left(\frac{(\mathbf{X}_{m+1} - \mathbf{X}_m)}{|\mathbf{X}_{m+1} - \mathbf{X}_m| |\mathbf{X}_m - \mathbf{X}_{m-1}|} - \frac{(\mathbf{X}_{m+1} - \mathbf{X}_m) \cdot (\mathbf{X}_m - \mathbf{X}_{m-1})}{|\mathbf{X}_{m+1} - \mathbf{X}_m|^3 |\mathbf{X}_m - \mathbf{X}_{m-1}|} (\mathbf{X}_m - \mathbf{X}_{m-1}) \right) (\delta_{m,l} - \delta_{m-1,l}) \right], \\ \frac{\partial \Delta s'(m)}{\partial \mathbf{X}_l} &= \frac{(\mathbf{X}_m - \mathbf{X}_{m-1})}{|\mathbf{X}_m - \mathbf{X}_{m-1}|} (\delta_{m,l} - \delta_{m-1,l}) + \frac{(\mathbf{X}_{m+1} - \mathbf{X}_m)}{|\mathbf{X}_{m+1} - \mathbf{X}_m|} (\delta_{m+1,l} - \delta_{m,l}). \end{aligned}$$

The variables $\mathbf{F}_{s,l}$ and $\mathbf{F}_{b,l}$ denote the discretized strain and bending forces exerted on the l th Lagrangian marker.

The discretized coupling energy of the elastic membrane can be written as

$$\mathcal{E}_c = \frac{\kappa_c}{2} \sum_{\mathbf{x}} (\psi - \mathcal{I})^2 (\Delta x)^d, \quad (35)$$

where $\sum_{\mathbf{x}}$ implies summation over all the Eulerian lattice nodes \mathbf{x} , and d is the domain dimensionality ($d = 2$ in the present case). The interfacial profile \mathcal{I} is given by Eq. (7). The corresponding discretized coupling force can then be obtained as

$$\begin{aligned} \mathbf{F}_{c,l} &= -\frac{\partial \mathcal{E}_c}{\partial \mathbf{X}_l} = -\sum_{\mathbf{x}} \frac{\delta f_{b,c}}{\delta \mathcal{I}} \frac{\partial \mathcal{I}}{\partial \mathbf{X}_l} \\ &= -\sum_{\mathbf{x}} \frac{\kappa_c}{4\alpha} (\psi - \mathcal{I}) \operatorname{sech}^2 \left(\frac{d(\mathbf{x}, \mathbf{X}_l)}{2\alpha} \right) \frac{\partial d(\mathbf{x}, \mathbf{X}_l)}{\partial \mathbf{X}_l}. \end{aligned} \quad (36)$$

The variable $\mathbf{F}_{c,l}$ represents the discretized coupling force exerted on the l th Lagrangian marker.

In the computational implementation, we exert the forces $\mathbf{F}_{s,l}$, $\mathbf{F}_{b,l}$, and $\mathbf{F}_{c,l}$ on each Lagrangian marker l .

C. Immersed boundary method

To reproduce the effect of $\mathbf{F}_{\text{mem},l}$ on the Eulerian fluid flow, denoted here by \mathbf{f}_{IB} , a spreading operation is used

$$\mathbf{f}_{\text{IB}}(\mathbf{x}, t) = \mathcal{S}[\mathbf{F}_{\text{mem},l}](\mathbf{x}) = \sum_{l=1}^{N_l} \mathbf{F}_{\text{mem},l} \delta_h(\mathbf{x} - \mathbf{X}_l) \Delta s. \quad (37)$$

The term δ_h denotes the discretized Dirac delta function, and the following formulation proposed by Peskin [56] is chosen here to perform the convolution in the spreading and interpolation operations

$$\delta_h(r) = \begin{cases} \frac{1}{8}(3 - 2|r| + \sqrt{1 + 4|r| - 4r^2}), & |r| \leq 1 \\ \frac{1}{8}(5 - 2|r| - \sqrt{-7 + 12|r| - 4r^2}), & 1 \leq |r| \leq 2 \\ 0, & 2 \leq |r|. \end{cases}$$

If the variable r is a vector, $\mathbf{r} = (r_x, r_y)$, then the two-dimensional δ_h is given by $\delta_h(\mathbf{r}) = \frac{1}{\Delta x^2} \delta_h(r_x/\Delta x) \delta_h(r_y/\Delta x)$.

Once the force \mathbf{f}_{IB} is computed, the total density ρ , auxiliary fields ϕ and ψ , and velocity \mathbf{v} fields can be obtained at the next time step $t + \Delta t$ by solving Eqs. (20) and (23). To calculate the forces $\mathbf{F}_{\text{mem},l}$ at $t + \Delta t$, the position of the Lagrangian markers \mathbf{X}_l , $l = 1, \dots, N_l$, at $t + \Delta t$ needs to be known. For this reason, the known $\mathbf{v}(\mathbf{x}, t + \Delta t)$ is interpolated at the Lagrangian markers as

$$\mathbf{U}(\mathbf{X}_l, t + \Delta t) = \mathcal{I}[\mathbf{v}](\mathbf{X}_l) = \sum_{\mathbf{x}} \mathbf{v} \delta_h(\mathbf{x} - \mathbf{X}_l) (\Delta x)^d. \quad (38)$$

The updated position of the Lagrangian markers can then be found by Euler's rule

$$\mathbf{X}_l(t + \Delta t) = \mathbf{X}_l(t) + \mathbf{U}(\mathbf{X}_l, t + \Delta t) \Delta t. \quad (39)$$

For simplicity, here we have used an explicit immersed boundary method. This is sufficient for the applications considered in this work. The temporal lag between the ternary fluid and elastic membrane can be eliminated by considering either subiterations of the coupled algorithm or implicit immersed boundary methods [57,58].

D. Surface Evolver

In the absence of closed-form solutions for nontrivial elastocapillary problems, we have benchmarked the proposed coupled lattice Boltzmann-immersed boundary method against a finite element approach, the SURFACE EVOLVER. SURFACE EVOLVER has been extensively used to model the equilibrium shapes of liquid interfaces and capillary forces [59–61], and model deformations of elastic membranes [62]. In SURFACE EVOLVER, the interfaces are discretized by triangulated meshes, and configurations in mechanical equilibrium correspond to minima of the total energy, obtained through a conjugate gradient descent method.

For our benchmarks, we model two-dimensional (2D) elastic capsules placed at a fluid-fluid interface in mechanical equilibrium. To minimize numerical deviations, the elastic capsules are initialized with exactly the same geometry as in the proposed model, described in Sec. IV A. The same free energy of the elastic membrane is implemented using the provided scripting language to formulate the strain and bending

energies as in Eqs. (29) and (30). In particular, the functions `edge_length` and `sqcurve_string_marked` are employed for the calculation of the strain and bending energies. The main difference is in the definition of the surface tensions; here, the corresponding energy is simply accounted for by adding a term proportional to the total length of each fluid or membrane interface, multiplied by a constant parameter matching the surface tension arising from the diffuse interface in the lattice Boltzmann method. No coupling energy has been considered, as both the elastic energies and surface tension are provided by the discrete representation of the capsule and the fluid-fluid interface. The constraint of conservation of the total capsule area has also been considered.

IV. RESULTS

The proposed fluid-structure solver is validated in Sec. IV A. The steady configuration of an elastic capsule positioned at a fluid-fluid interface is chosen for this purpose. We perform a thorough comparison with the reference results of SURFACE EVOLVER for different cases of surface tension ratios, and various combinations of stretching and bending moduli. We also establish the Galilean invariance of the governing equations of the ternary fluid and elastic structure. Finally, a more complex configuration is considered in Sec. IV B to demonstrate the capabilities of the proposed model.

A. Elastic capsule at fluid-fluid interface

To benchmark the proposed model, the configuration of an elastic capsule placed at a fluid-fluid interface, as shown in Fig. 1(a), is studied. An initially circular capsule of radius R is located at the center of a computational domain of dimensions $12R \times 6R$. The capsule relaxes to a mechanical equilibrium shape, which depends on the balance of the elastic strain and bending forces and the surface tensions γ_{12} , γ_{13} , and γ_{23} . To quantify the capsule deformation, we employ the Taylor deformation $D = (L - B)/(L + B)$, where L and B are, respectively, the major and minor axes of the final elliptical capsule shape. Periodic boundary conditions are considered at all the domain boundaries. Simulations are performed for several combinations of stretching and bending moduli, $\kappa_s = \{10^{-3}, 10^{-2}, 10^{-1}\}$ and $\kappa_b = \{10^{-4}, 10^{-2}\}$. We consider two cases: (1) $\gamma_{13} = \gamma_{23}$, resulting in a capsule shape that is symmetrical along the domain center lines, and (2) $\gamma_{13} \neq \gamma_{23}$, resulting in the capsule to be more immersed in one of the surrounding fluid phases. We will refer thereafter to case 1 as the symmetric case, and case 2 as the asymmetric one. In the symmetric case, the parameters κ_1 and κ_2 are both taken equal to 0.008, while the parameter κ_3 ranges from 0.0005 to 0.01 with a step size of 0.0005. The surface tension ratio $\gamma_{12}/\gamma_{13} = \gamma_{12}/\gamma_{23}$, varying from 0.888 to 1.882, is considered. In the asymmetric case, we assign the parameters κ_1 and κ_2 to, respectively, be 0.008 and 0.002, while the parameter κ_3 varies from 0.0005 to 0.008 in steps of 0.0005. The corresponding surface tension ratio $\gamma_{13} = \gamma_{23}$, ranging from 1.60 to 3.40, is examined. Both the relaxation times and the parameters Γ_ϕ , Γ_ψ are all considered to be equal to 1, $\tau = \tau_\phi = \tau_\psi = 1$, and $\Gamma_\phi = \Gamma_\psi = 1$.

We first investigate the effect of the free-energy parameter α on the capsule dynamics and flow field in both the

TABLE I. Taylor deformation D and relative error δD with respect to the reference solution obtained by SURFACE EVOLVER at different values of the parameter α for the symmetric and asymmetric cases. The elastic capsule is initialized with radius $R = 20$. The coupling coefficient is set to be $\kappa_c = 10^{-2}$.

α	Symmetric		Asymmetric	
	D	$\delta D(\%)$	D	$\delta D(\%)$
1.0	0.489	8.43	0.392	5.31
1.5	0.505	5.43	0.403	2.66
2.0	0.508	4.87	0.410	0.97
Ref.	0.534		0.414	

symmetric and asymmetric cases. Simulations are conducted here for the most deformable capsule, that is $\kappa_s = 10^{-3}$, at a bending modulus $\kappa_b = 10^{-2}$ and the highest surface tension ratio studied in each case, namely, $\gamma_{12}/\gamma_{13} = 1.882$ and $\gamma_{13}/\gamma_{23} = 3.40$. The elastic capsule is initialized with radius $R = 20$. The coupling coefficient is kept constant at $\kappa_c = 10^{-2}$. The comparison of the Taylor deformation D and the corresponding relative error $\delta D = |D_{\text{Ref}} - D|/D_{\text{Ref}}$, where D_{Ref} is the reference solution obtained by SURFACE EVOLVER, at the various parameters α is shown in Table I. At $\alpha = 1$, the Taylor deformation is highly underpredicted, with the relative error being greater than 5% in both the symmetric and asymmetric cases. The relative difference falls below 5% in both cases only at $\alpha = 2$. It is worth noting that the magnitude of the spurious currents decreases from approximately 5×10^{-5} to 2×10^{-5} when increasing the parameter α from 1 to 2. As seen from Eqs. (5) and (7), the parameter α has an effect on the interfacial profile for the density of the fluid components as well as the one across the elastic capsule. To assess this effect, the capsule shape is plotted along with the contour lines of $C_3 = \psi = 0.5$ and $\mathcal{I} = 0.5$ at the various values of the parameter α for the symmetric case in Fig. 3. For the optimal values of α and κ_c , the elastic capsule should be positioned at the middle of the interfacial profile \mathcal{I} , which in turn should be superimposed onto the middle of the interfacial profile for C_3 . As observed from Fig. 3, the elastic capsule is indeed located at $\mathcal{I} = 0.5$ for all values of α . However, deviations between the contour lines of $\psi = 0.5$ and $\mathcal{I} = 0.5$ can be noticed close to the three-phase contact point for the lower values of α . These contour lines agree well with each other only for $\alpha = 2$. This establishes our choice of $\alpha = 2$ in subsequent simulations. Similar observations can be made in the asymmetric case (data not shown). It is also worth noting that the suitable choice for α will be affected by the form of the discretized Dirac delta function in the immersed boundary approach.

To examine the effect of the coupling coefficient on the superposition of the interfacial profiles of ψ and \mathcal{I} , we perform simulations varying the value of κ_c from 5×10^{-3} to 5×10^{-2} . As before, capsules of initial radius $R = 20$ are considered. Figure 4 shows the capsule's position in conjunction with the contour lines of $\psi = 0.5$ and $\mathcal{I} = 0.5$ for the symmetric case. Similar to before, the elastic capsule is placed at $\mathcal{I} = 0.5$ for all values of κ_c . Significant discrepancies between the contour lines of $\psi = 0.5$ and $\mathcal{I} = 0.5$ can be observed not only close to the three-phase contact point, but at

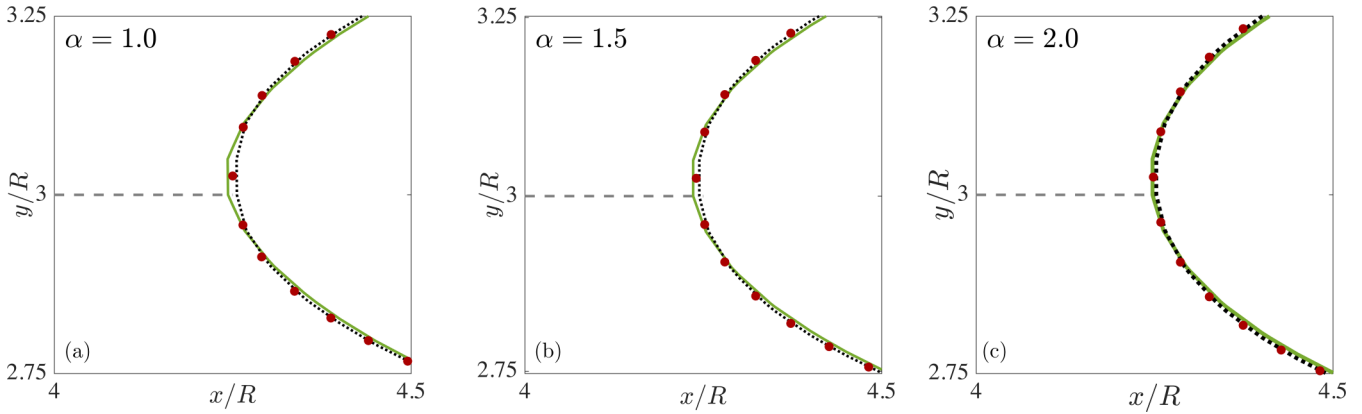


FIG. 3. Comparison of the elastic capsule’s position (filled circles) and contours of $\psi = 0.5$ (solid lines) and $\mathcal{I} = 0.5$ (dotted lines) for (a) $\alpha = 1.0$, (b) $\alpha = 1.5$, and (c) $\alpha = 2.0$ in the symmetric case. The shown results correspond to a capsule of initial radius $R = 20$, considering a coupling coefficient of $\kappa_c = 10^{-2}$. The middle of the diffuse interface distinguishing fluids 1 and 2 is illustrated by dashed lines.

the entirety of these contour lines for $\kappa_c = 5 \times 10^{-3}$. For $\kappa_c = 10^{-2}$, the desired contour lines agree well with each other, as previously mentioned. This coupling coefficient value is the threshold for the contour lines to overlap. For the highest coupling coefficient value shown here, that is $\kappa_c = 5 \times 10^{-2}$, the contour lines of $\psi = 0.5$ and $\mathcal{I} = 0.5$ are perfectly superposed. However, this value of κ_c was found to be close to the threshold before the domination of the coupling energy over the rest of the free-energy terms occurs. To avoid numerical instabilities, the use of $\kappa_c = 10^{-2}$ in following simulations was deemed appropriate. Similar trends have been observed in the asymmetric case (data not shown).

To isolate the effect of increasing capsule radius on the Taylor deformation and capsule shape, simulations are carried out varying the value of R , while keeping constant the ratio of the elastocapillary length $l_{EC} = \sqrt{\kappa_b/\gamma_{12}}$ to the capsule’s radius. Table II demonstrates the Taylor deformation and the matching relative error along with the normalized major and minor axes at the different values of the radius R . Let us examine first the symmetric case. In the coarsest mesh ($R = 10$), the Taylor deformation predicted by our numerical framework has a relative difference to the reference solution of slightly higher than 10%. The relative error drops below 5% in the finer meshes. This observation is visualized in Fig. 5(a). Due

to the symmetry along the vertical center line, only one-half of the capsule shapes is displayed at $R = 10$, 20, and 40, after which the differences in the Taylor deformation and capsule shape are negligible. At $R = 10$, the capsule width is sufficiently captured, and slight differences with respect to the normalized B found in the finer meshes can be observed. The capsule length is, however, under-resolved in the coarsest mesh. The capsule shape obtained for $R = 20$ agrees well with the finest mesh one, with the two shapes differing noticeably only in the proximity of the three-phase contact point. In the asymmetric case, the relative difference in Taylor deformation displays nonmonotonic behavior with an increase in R , despite both the normalized capsule length and width converging towards the reference values. This indicates that the Taylor deformation should not be considered as the sole convergence criterion (since different combinations of L/R and B/R may result in the same D), but in conjunction with the specific capsule length and width values and its shape. In Fig. 5(b), it can be seen that the capsule shape corresponding to the coarsest mesh exhibits evident differences with respect to those of the finer meshes and the reference solution. Discrepancies can be noticed close to the three-phase contact point as well as in the capsule part immersed in fluid 2. The capsule shapes of the finer meshes are in good accordance between them and with

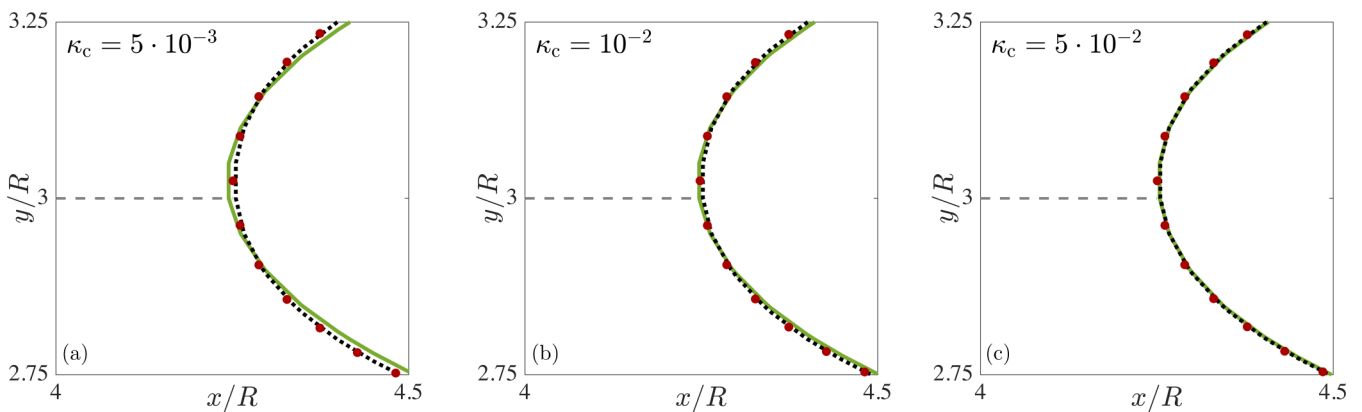


FIG. 4. Comparison of the elastic capsule’s position (filled circles) and contours of $\psi = 0.5$ (solid lines) and $\mathcal{I} = 0.5$ (dotted lines) for (a) $\kappa_c = 5 \times 10^{-3}$, (b) $\kappa_c = 10^{-2}$, and (c) $\kappa_c = 5 \times 10^{-2}$ in the symmetric case. The presented results correspond to a capsule of initial radius $R = 20$, with the parameter α being equal to 2.0. The dashed lines denote the middle of the diffuse interface separating fluids 1 and 2.

TABLE II. Taylor deformation D , relative error δD , and normalized major L and minor B axes at different capsule radii R for the symmetric and asymmetric cases. $\alpha = 2$ and coupling coefficient $\kappa_c = 10^{-2}$ are considered here.

R	Symmetric				Asymmetric			
	D	$\delta D(\%)$	L/R	B/R	D	$\delta D(\%)$	L/R	B/R
10	0.476	10.9	3.34	1.19	0.413	0.2	3.07	1.27
20	0.508	4.9	3.55	1.16	0.410	1.0	3.10	1.30
30	0.513	3.9	3.61	1.16	0.406	1.9	3.10	1.31
40	0.518	3.0	3.65	1.16	0.412	0.5	3.12	1.30
50	0.519	2.8	3.66	1.16	0.412	0.5	3.12	1.30
Ref.	0.534		3.77	1.14	0.414		3.16	1.31

the reference shape. As the relative errors between $R = 20$ and 40 are only $\sim 2\%$ and 0.5% in the symmetric and asymmetric cases, we have decided to perform subsequent simulations considering $R = 20$.

We subsequently explore the performance of our numerical scheme on various combinations of stretching and bending moduli and surface tension ratios. Figure 6 shows the Taylor deformations obtained by our simulations, whose results are represented by lines, compared to the ones measured by SURFACE EVOLVER, denoted by dot symbols. As expected, the variations in the Taylor deformation found for a particular combination of κ_s and κ_b become more apparent with a decrease in the stretching modulus. For stiff capsules, that is $\kappa_s \geq 10^{-1}$, the capsule deformation reaches a plateau for high surface tension ratios. On the contrary, the results for highly deformable capsules, that is $\kappa_s \leq 10^{-3}$, tend to the ones obtained for the pure liquid lens configuration, depicted by filled square symbols. Here, a liquid lens is formed when a droplet of fluid 3 is suspended at the interface between fluids 1 and 2. Its shape and size depend on the force balance between the surface tensions at the three-phase contact line. It is also obvious that the effect of the bending coefficient on the capsule deformation is negligible for a given stretching modulus. Our results agree well with those of SURFACE EVOLVER, with a typical relative error in D of approximately 5.6% in both the symmetric and asymmetric cases. These discrepancies in the Taylor deformation could be dampened by increasing the

computational domain size and potentially the parameter α , as demonstrated earlier, with an increase though in the computational cost.

To illustrate the effect of these discrepancies on the mechanical equilibrium shape of the elastic capsule, the latter is plotted for different combinations of κ_s and κ_b at the highest surface tension ratios studied here, that is, $\gamma_{12}/\gamma_{13} = 1.882$ in the symmetric case and $\gamma_{13}/\gamma_{23} = 3.40$ in the asymmetric one, as presented in Fig. 7. For stiff and moderately deformable capsules, corresponding to $\kappa_s = 10^{-1}$ and $\kappa_s = 10^{-2}$, an excellent agreement is observed between our simulation results and those of SURFACE EVOLVER. No notable differences can be seen in the capsule shapes obtained by our numerical model and SURFACE EVOLVER close to the three-phase contact point. For highly deformable capsules, a slightly elongated shape is obtained by the reference software compared to the one found by our fluid-structure solver. Deviations close to the three-phase contact point could be attributed to the considerable membrane curvature, as the curvature radius reduces and becomes comparable to the interface width. The capsule width, however, matches well.

We finally prove the Galilean invariance of the proposed model. To do so, simulations are performed in an inertial frame of reference, and their results are compared to the ones obtained by the previous stationary simulations. At $t = 0$, all the fluid components are given a constant horizontal velocity $U_{x,0}$. Due to the fluid-structure interaction, the initially

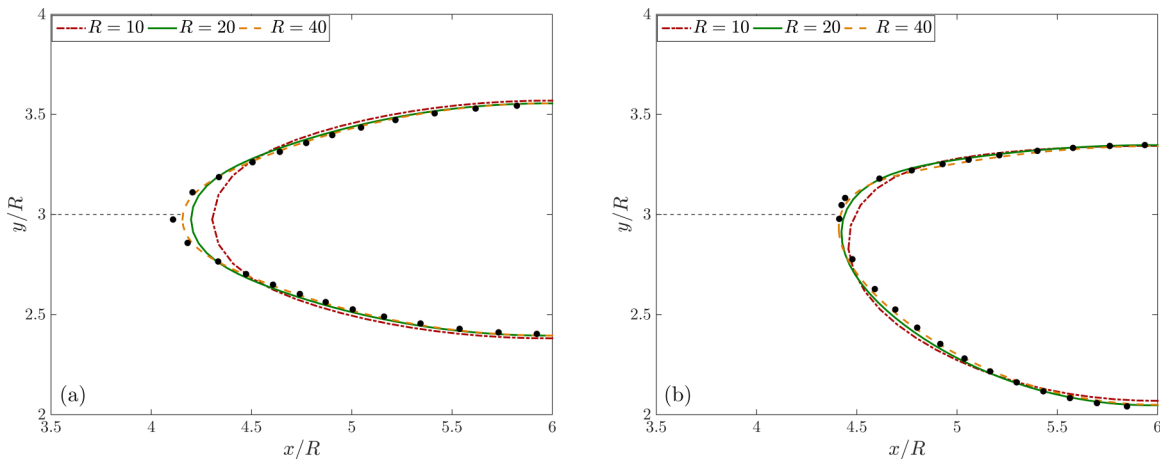


FIG. 5. Mechanical equilibrium shapes of the elastic capsule with different radii R for the (a) symmetric, and (b) asymmetric cases. Our results are compared to the reference capsule shapes obtained by SURFACE EVOLVER (filled circles). For viewing clarity, the reference capsule shapes are subsampled by a factor of 4. The dashed lines depict the middle of the diffuse interface separating fluids 1 and 2.

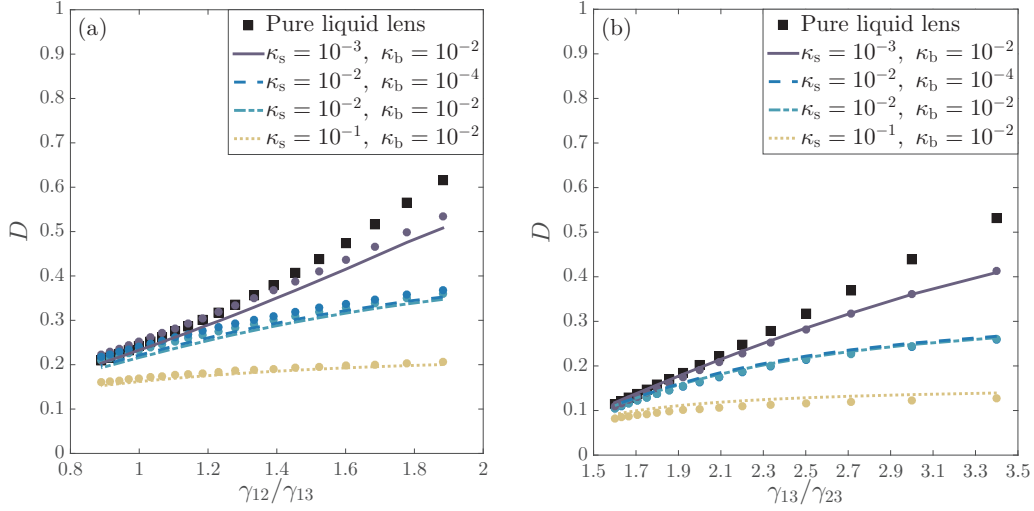


FIG. 6. Comparison of the Taylor deformation D between the results of the fluid-structure solver (solid lines) and SURFACE EVOLVER (filled circles) for (a) the symmetric case, and (b) the asymmetric one. The results of the fluid solver for the pure liquid lens configuration are also presented (filled squares).

circular capsule travels in the same direction with an equal velocity. Three different velocity values are tested here: $U_{x,0} = \{10^{-4}, 10^{-3}, 10^{-2}\}$. The Galilean invariance is checked in both the symmetric and asymmetric (data not shown) cases for $\kappa_s = 10^{-3}$ and $\kappa_b = 10^{-2}$ at the highest surface tension ratios examined, respectively, here. The shapes of the elastic capsule, after the capsule reaches mechanical equilibrium in the inertial reference frame, found for the different velocities are compared to each other and to the ones of the corresponding stationary simulations. These comparisons can be seen in Fig. 8. In both cases, the results for the capsule shapes in the moving and stationary frames are superposed, indicating that the proposed model is Galilean invariant.

B. Capillary bridge between two elastic capsules

To show the capabilities of our model, the configuration of a capillary bridge formed between two deformable capsules, as shown in Fig. 9(a), is now investigated. Two initially circular capsules of radius $R = 20$ are placed at $(x_{c1}, y_{c1}) = (9R/2, 3R)$ and $(x_{c2}, y_{c2}) = (15R/2, 3R)$ of a computational

domain of dimensions $12R \times 6R$. The capillary bridge, composed of the fluid component 2, is initialized as a rectangular area of dimensions $2S \times H_b = R \times 31R/10$ located at the center of the computational domain. Both the capillary bridge and elastic capsules are surrounded by the fluid component 1. Due to the presence of the surface tensions γ_{12} , γ_{13} , and γ_{23} as well as the elastic strain and bending forces, the capsules relax to a deformed mechanical equilibrium shape depending on the forces' balance. This mechanical equilibrium shape depends also on the initial distance between the two capsules, $2S$, and the volume of the capillary bridge. To confine the parameter space of the current study, all the simulations are performed only for a dimensionless initial distance $S' = 2S/R = 1$ and a relative area $A_{rel} = A_b/A_c \approx 1.02$, where A_b and A_c are the areas of the capillary bridge and elastic capsules. Three different surface tension ratios are tested here, $\gamma_{12}/\gamma_{13} \approx \{0.57, 0.67, 0.80\}$, where the parameters κ_1 , κ_2 and κ_3 are, respectively, taken equal to $\kappa_1 = \{0.001, 0.003, 0.009\}$, $\kappa_2 = 0.003$ and $\kappa_3 = 0.006$. The parameter α is set to be $\alpha = 2$. The simulations are performed for various stretching moduli $\kappa_s = \{10^{-4}, 10^{-3}, 10^{-2}, 10^{-1}, 10^0\}$ and constant bending

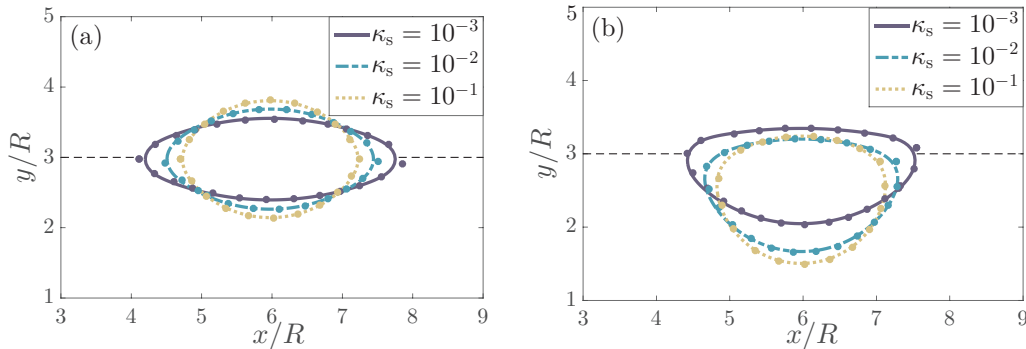


FIG. 7. Mechanical equilibrium shapes of the elastic capsule with $\kappa_b = 10^{-2}$ for the (a) symmetric and (b) asymmetric cases. The results of our simulations (solid lines) are compared to those of SURFACE EVOLVER (filled circles), which are subsampled by a factor of 4 for viewing clarity. The dashed lines represent the middle of the diffuse interface separating fluids 1 and 2.

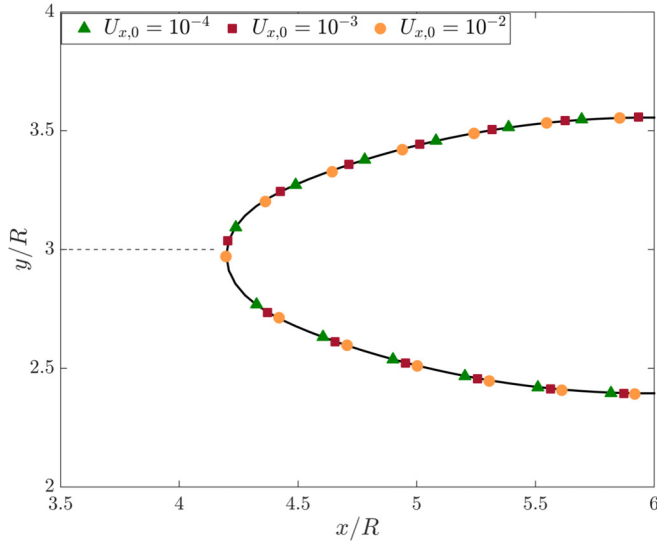


FIG. 8. Comparison of the capsule shapes between the stationary (solid lines) and inertial reference frames for the symmetric case. For viewing clarity, the Lagrangian markers depicted here for the results in the inertial reference frame are subsampled by a factor of 5. The middle of the diffuse interface separating fluids 1 and 2 is denoted by dashed lines.

and coupling coefficients $\kappa_b = 10^{-2}$ and $\kappa_c = 10^{-2}$. As before, $\tau = \tau_\phi = \tau_\psi = 1$ and $\Gamma_\phi = \Gamma_\psi = 1$. Periodic boundary conditions are applied at all the domain boundaries. At the converged state, the dimensionless aspect ratio of the elastic capsules can be defined as L_c/H_c .

The effect of stretching modulus on the aspect ratio of the capsules is presented in Fig. 10 for the different surface tension ratios. For low γ_{12}/γ_{13} , the capsules seem to take similar mechanical equilibrium shapes independently of their degree of elasticity. For moderate and high γ_{12}/γ_{13} , the aspect ratio changes significantly between stiff and moderately deformable ($\kappa_s = 10^{-2}$) capsules, while it reaches a plateau for highly deformable ($\kappa_s \leq 10^{-3}$) capsules. It can also be noted that the surface tension ratio affects considerably the capsules' aspect ratio for a given stretching modulus. This can be clearly seen in Fig. 9(b), where the mechanical equilibrium shapes of the highly deformable ($\kappa_s = 10^{-3}$) capsules are plotted for the different γ_{12}/γ_{13} . At $\gamma_{12}/\gamma_{13} \approx 0.57$, the capsules retain an almost circular shape, having only the part of their surface coming in contact with the capillary bridge slightly compressed. As the surface tension ratio increases, the capsules move towards each other, taking a semicircular shape and causing the formation of a narrower and higher capillary bridge. Despite the fact that the stretching modulus has a notable effect on the aspect ratio of the elastic capsules at high γ_{12}/γ_{13} , the corresponding variations in their shapes are small for different κ_s , as shown in Fig. 9(c). The capsule becomes slightly shorter and wider with an increase in κ_s .

Finally, the transient shapes of the highly deformable capsules at a surface tension ratio $\gamma_{12}/\gamma_{13} \approx 0.80$ are shown in Fig. 11. For clarity, we present only the results of the left-hand side capsule; the transient shapes of the right-hand side capsule are symmetric to the ones presented across the vertical center line. As mentioned previously, the elastic capsules have

initially, at $t_0 = 0$, a circular shape. It is worth noting that the capsules take quickly, already at $t = 5 \times 10^3$, a semicircular shape similar to the mechanical equilibrium one. As the time passes, the capsules become narrower and more elongated along the x and y axis, respectively. Minimal changes in the capsules shapes can be observed between $t = 1 \times 10^5$, which corresponds to half of the total simulation time, and $t = 2 \times 10^5$, where the capsules are considered to have reached the mechanical equilibrium shape.

V. CONCLUSIONS

In this work, we have presented a modeling technique for the coupling of a multicomponent fluid flow with deformable, infinitely thin structures. For the sake of simplicity, we have considered the case where elastic membranes enclosing a fluid component 3 are immersed in a two-component phase flow consisted of fluids 1 and 2. For this case, we have introduced a modified formulation of the free energy of the ternary fluid, taking into consideration its interaction with the elastic membranes, to the original one proposed by Semprebon *et al.* [45]. Taking advantage of the laws of thermodynamics, we have also derived the governing equations of motion for the fluid and the membrane.

The macroscopic equations of motion of the fluid-structure system are solved here by a partitioned numerical approach. This approach consists of a mesoscopic lattice Boltzmann method for resolving the ternary fluid flow in an Eulerian description, a finite difference method to evolve the membranes equations of motion in a Lagrangian framework, and an immersed boundary method to couple the Eulerian and Lagrangian solvers. The fluid and structure solvers are coupled through a forcing source term in the lattice Boltzmann equation, acting as a feedback of the structure's response on the flow.

We have subsequently validated our computational algorithm against SURFACE EVOLVER, an open-source software capable of modeling steady liquid surface problems employing an energy minimization approach. The configuration of an elastic capsule placed at a fluid-fluid interface was considered as the benchmark test. We have compared in detail the equilibrium shapes of the capsule, and its corresponding deformation parameters for different scenarios of the surface tensions and combinations of the capsule's stretching and bending moduli. An overall good agreement has been observed between our results and the reference ones. We have also demonstrated the Galilean invariance of our model equations. Finally, our algorithm has been applied to a more complex configuration, that is, the capillary bridge formed between two elastic capsules. Although an extensive investigation of the parameter space was beyond the scope of this work, it should be noted that this configuration is a particularly rich phenomenon, where the criteria for the bridge rupture and the case of unequal capsules are worth being studied in the future. Importantly, the proposed model also enables the study of dynamic configurations.

We have assumed here that all fluid components have the same density and viscosity. By modifying the Landau free-energy functional \mathcal{E}_f of Eq. (2) in an appropriate way [46] and following a rationale similar to the one presented in Sec. II,

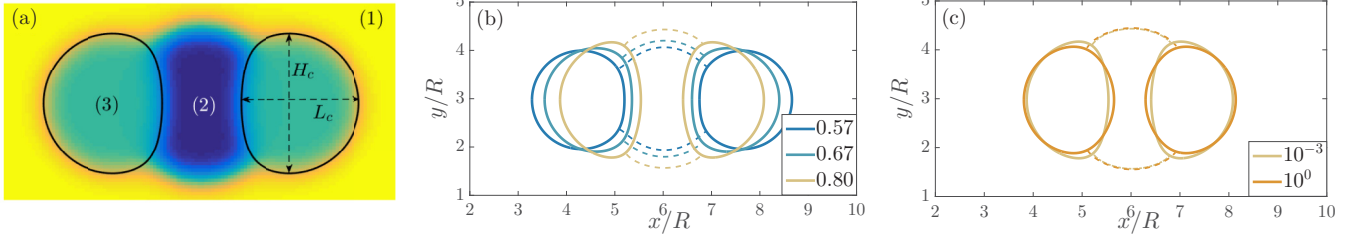


FIG. 9. (a) Schematic diagram of a capillary bridge, composed of fluid (2), formed between two elastic membranes (solid lines), enclosing the fluid component (3), while suspended in fluid (1). Comparison of the mechanical equilibrium shapes of the elastic capsules for (b) different surface tension ratios γ_{12}/γ_{13} at $\kappa_s = 10^{-3}$, and (c) different stretching moduli κ_s at $\gamma_{12}/\gamma_{13} \approx 0.80$. The dashed lines depict the capillary bridge boundaries.

our model could be extended to the case where the components of the ternary fluid mixture have different densities. Extension to multicomponent fluids of variable viscosity is straightforward. External forces, such as gravity, can be readily taken into consideration by assigning $\mathbf{f}_{\text{ext}} \neq \mathbf{0}$ in Eq. (27). Extension to three dimensions is planned for the future, which will enable us to deal with more complex and realistic configurations encountered in experiments. The model could also be generalized so as to include more fluid components enclosed in or surrounding the elastic membranes, allowing us to tackle a wider range of applications, for example, capsules containing multiple phases [16,17]. In addition, the formulations of the strain and bending energies could be modified to consider materials obeying different constitutive laws, such as nonlinear hyperelastic materials or biological membranes. Finally, the structure solver could be adapted in order to simulate open surfaces, encountered for instance in the wetting of a soft substrate [20,21].

ACKNOWLEDGMENTS

We would like to thank Professor K. Brakke for his assistance in implementing our free-energy model of the elastic

membranes in SURFACE EVOLVER. M.P. and H.K. acknowledge EPSRC (Grant No. EP/P007139/1) for funding. A.C.M.S. is grateful to the EPSRC Centre for Doctoral Training in Soft Matter and Functional Interfaces (Grant No. EP/L015536/1) for financial support. T.K. acknowledges support from the award of a Chancellor’s Fellowship from the University of Edinburgh. C.S. acknowledges support from Northumbria University through the Vice-Chancellor’s Fellowship Programme and EPSRC (Grant No. EP/S036857/1) for funding. C.S. and T.K. acknowledge the support by the late Jason Reese.

APPENDIX: DERIVATION OF THE EQUATIONS OF MOTION OF TERNARY FLUIDS IN INTERACTION WITH ELASTIC MEMBRANES

1. Entropy equation

The first law of thermodynamics can be formulated as

$$\frac{d(U + E)}{dt} = \frac{dW}{dt} + \frac{dQ}{dt}, \quad (\text{A1})$$

where t is time, U and E are, respectively, the internal and kinetic energies, W is the work done on the ternary fluid

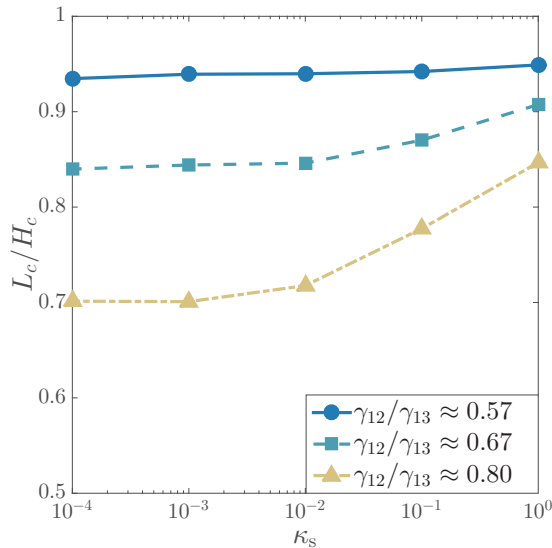


FIG. 10. Aspect ratio L_c/H_c of the elastic capsules as a function of stretching modulus κ_s at different surface tension ratios γ_{12}/γ_{13} .

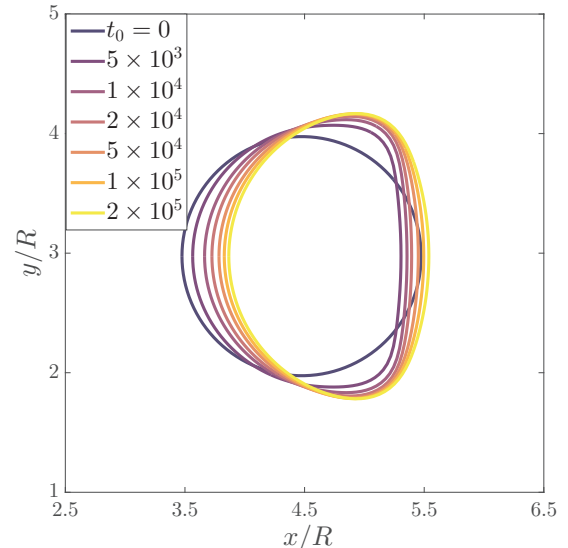


FIG. 11. Shapes of the highly ($\kappa_s = 10^{-3}$) deformable capsule at $\gamma_{12}/\gamma_{13} \approx 0.80$ at different time steps t .

system by its surroundings, and Q denotes the amount of heat supplied to the system for its temperature T to be kept constant. The total entropy S can be split into two parts: the entropy of the system S_{sys} and the entropy of its surroundings S_{sur} . By definition, the total free energy of the system can be expressed as

$$F = U - TS_{\text{sys}}. \quad (\text{A2})$$

It is also known that the entropy of the system's surroundings is related to the heat Q by

$$dS_{\text{sur}} = -\frac{dQ}{T}. \quad (\text{A3})$$

Taking into account Eqs. (A1)–(A3), it can be shown that

$$\frac{dS}{dt} = \frac{dS_{\text{sys}}}{dt} + \frac{dS_{\text{sur}}}{dt} = -\frac{1}{T} \frac{d(F+E)}{dt} + \frac{1}{T} \frac{dW}{dt}. \quad (\text{A4})$$

Here, the system of interest consists of the ternary fluid (denoted by subscript f) and the membrane. Let us first concentrate on the terms related to the ternary fluid.

Given the simulation volume V , the free and kinetic energies of the ternary fluid can be defined as

$$F_f = \int_V f_f dV, \quad E_f = \frac{1}{2} \int_V \rho |\mathbf{u}|^2 dV, \quad (\text{A5})$$

where f_f is the free-energy density of the ternary fluid, ρ is the total mass density of the fluid mixture, and \mathbf{u} denotes the mass-averaged velocity. The fluid free-energy density is the sum of two contributions: a free-energy density of the bulk fluid f_b , and a local free-energy density gradient contribution f_{∇} allowing the existence of diffuse fluid-fluid interfaces

$$f_f = f_b + f_{\nabla}. \quad (\text{A6})$$

The interfacial free-energy density term is defined here as

$$f_{\nabla} = \frac{1}{2} \sum_{m,n=1}^N c_{mn} \nabla C_m \cdot \nabla C_n, \quad (\text{A7})$$

where N denotes the number of components of the fluid mixture ($N = 3$ here), c_{mn} is the cross influence parameter, and C_m represents the concentration fraction of fluid m ($m = 1, 2, 3$). The total mass density is given by

$$\rho = \sum_{m=1}^N C_m M_{w,m}, \quad (\text{A8})$$

where $M_{w,m}$ denotes the weight of component m .

Following the rationale of Kou and Sun [52], we can obtain expressions for dF_f/dt and dE_f/dt , by applying the Reynolds transport and Gauss divergence theorems to Eq. (A5), identical to those in [52], and the mass conservation law of the fluid mixture

$$\frac{\partial \rho}{\partial t} + \nabla \cdot (\rho \mathbf{u}) + \sum_{m=1}^N M_{w,m} \nabla \cdot \mathbf{J}_m = 0. \quad (\text{A9})$$

$\mathbf{J}_m = M_m \nabla \mu_m$ denotes the diffusion flux of component m , and M_m represent the corresponding mobility parameters. The chemical potential μ_m is discussed in Sec. II C.

The rate of change of the work done by the force \mathbf{F}_{sur} is given by

$$\frac{dW}{dt} = \int_{\partial V} (\mathbf{F}_{\text{sur}} \cdot \mathbf{u}) ds, \quad (\text{A10})$$

where the integration takes place over the volume's surface boundary ∂V . The force \mathbf{F}_{sur} is related to the Cauchy stress tensor $\boldsymbol{\sigma}$ of the ternary fluid by $\mathbf{F}_{\text{sur}} = -\boldsymbol{\sigma} \cdot \mathbf{n}$, where \mathbf{n} denotes the outward unit normal vector of V . Equation (A10) can thus take the form

$$\begin{aligned} \frac{dW}{dt} &= - \int_{\partial V} [(\boldsymbol{\sigma} \cdot \mathbf{n}) \cdot \mathbf{u}] ds \\ &= - \int_V [\boldsymbol{\sigma}^T : \nabla \mathbf{u} + \mathbf{u} \cdot (\nabla \cdot \boldsymbol{\sigma})] dV, \end{aligned} \quad (\text{A11})$$

where $\boldsymbol{\sigma}^T$ denotes the transpose of $\boldsymbol{\sigma}$.

By making use of the expressions for dF_f/dt , dE_f/dt , and dW/dt , the terms on the right-hand side of Eq. (A4) related to the ternary fluid can be collected as follows:

$$\begin{aligned} & - \frac{d(F_f + E_f)}{dt} + \frac{dW}{dt} \\ &= \int_V \left[-\frac{\partial f_f}{\partial t} - \nabla \cdot (f_f \mathbf{u}) + \frac{1}{2} \sum_{m=1}^N M_{w,m} \nabla \cdot [(\mathbf{u} \cdot \mathbf{u}) \mathbf{J}_m] \right. \\ & \quad \left. - \boldsymbol{\sigma}^T : \nabla \mathbf{u} - \mathbf{u} \cdot \left(\rho \frac{d\mathbf{u}}{dt} + \sum_{m=1}^N M_{w,m} \mathbf{J}_m \cdot \nabla \mathbf{u} + \nabla \cdot \boldsymbol{\sigma} \right) \right] dV, \end{aligned} \quad (\text{A12})$$

where $\frac{d\mathbf{u}}{dt}$ is the total derivative of \mathbf{u} , defined as $\frac{\partial \mathbf{u}}{\partial t} + \mathbf{u} \cdot \nabla \mathbf{u}$.

2. Transport equation of the free-energy density of the ternary fluid

The pressure p of the fluid mixture can be defined as

$$p = \sum_{m=1}^N C_m \mu_m - f_f, \quad (\text{A13})$$

where μ_m is the chemical potential of component m , given by

$$\mu_m = \frac{\delta f_f}{\delta C_m} = \mu_m^b - \underbrace{\sum_{n=1}^N \nabla \cdot (c_{mn} \nabla C_n)}_{\mu_m^{\nabla}}, \quad (\text{A14})$$

where $\mu_m^b = \frac{\delta f_b}{\delta C_m}$ and $\mu_m^{\nabla} = \frac{\delta f_{\nabla}}{\delta C_m}$ stand for the bulk and interfacial chemical potentials of component m . Due to Eq. (A14), Eq. (A13) can be rewritten as

$$\begin{aligned} p &= \underbrace{\sum_{m=1}^N C_m \mu_m^b}_{p_b} - f_b - \sum_{m,n=1}^N C_m \nabla \cdot (c_{mn} \nabla C_n) \\ & \quad - \frac{1}{2} \sum_{m,n=1}^N c_{mn} \nabla C_m \cdot \nabla C_n. \end{aligned} \quad (\text{A15})$$

The bulk pressure p_b can be further divided into two parts: $p_{b,f}$ accounting for the contribution of the bulk free-energy density owing to the chosen free-energy functional $f_{b,f}$ of the fluid

mixture, and $p_{b,c}$ taking into account the contribution of the bulk free-energy density due to a fluid-membrane coupling-energy functional $f_{b,c}$:

$$p_b = \underbrace{\sum_{m=1}^N C_m \mu_m^{b,f} - f_{b,f}}_{p_{b,f}} + \underbrace{C_3 \frac{\delta f_{b,c}(C_3, \mathcal{I})}{\delta C_3} - f_{b,c}}_{p_{b,c}}, \quad (\text{A16})$$

where $f_b = f_{b,f} + f_{b,c}$ and $\mu_m^{b,f} = \frac{\delta f_{b,f}(C_m)}{\delta C_m}$. The coupling-energy functional $f_{b,c}$ depends only on the component enclosed in the membrane, which is assumed to be fluid 3 in this work, and an interfacial profile \mathcal{I} across the elastic membrane for the ternary fluid. It should be noted that the term $p_{b,c}$ on the right-hand side of Eq. (A16) differentiates the present model from the multicomponent flow model proposed by Kou and Sun [52], as the latter does not account for $f_{b,c}$. The gradient of the bulk pressure can be found as

$$\begin{aligned} \nabla p_b &= \nabla \left(\sum_{m=1}^N C_m \mu_m^b - f_b \right) \\ &= \sum_{m=1}^N (\mu_m^b \nabla C_m + C_m \nabla \mu_m^b) - \sum_{m=1}^N \mu_m^b \nabla C_m - \frac{\delta f_b}{\delta \mathcal{I}} \nabla \mathcal{I} \\ &= \sum_{m=1}^N C_m \nabla \mu_m^b - \frac{\delta f_{b,c}}{\delta \mathcal{I}} \nabla \mathcal{I}. \end{aligned} \quad (\text{A17})$$

It can also be shown that

$$\begin{aligned} \nabla p_{b,c} - C_3 \nabla \left(\frac{\delta f_{b,c}}{\delta C_3} \right) \\ = \nabla \left(C_3 \frac{\delta f_{b,c}}{\delta C_3} - f_{b,c} \right) - C_3 \nabla \left(\frac{\delta f_{b,c}}{\delta C_3} \right) = - \frac{\delta f_{b,c}}{\delta \mathcal{I}} \nabla \mathcal{I}. \end{aligned} \quad (\text{A18})$$

Taking into account the above, the time derivative of the bulk f_b free-energy density can be deduced as

$$\begin{aligned} \frac{\partial f_b}{\partial t} &= \sum_{m=1}^N \mu_m^b \frac{\partial C_m}{\partial t} + \frac{\delta f_b}{\delta \mathcal{I}} \frac{\partial \mathcal{I}}{\partial t} \\ &= -p_b \nabla \cdot \mathbf{u} - \mathbf{u} \cdot \left[\nabla p_{b,c} - C_3 \nabla \left(\frac{\delta f_{b,c}}{\delta C_3} \right) \right] \\ &\quad - \nabla \cdot (f_b \mathbf{u}) - \sum_{m=1}^N \mu_m^b \nabla \cdot \mathbf{J}_m + \frac{\delta f_{b,c}}{\delta \mathcal{I}} \frac{\partial \mathcal{I}}{\partial t}, \end{aligned} \quad (\text{A19})$$

where the second and last terms on the right-hand side of Eq. (A19) are introduced here due to the presence of the elastic membrane, not being included in the corresponding expression in [52]. The time derivative and divergence of the interfacial f_{∇} free-energy density are formulated similarly to those in [52]. The transport equation of the free-energy density f_f of the ternary fluid can then be found as

$$\begin{aligned} \frac{\partial f_f}{\partial t} + \nabla \cdot (f_f \mathbf{u}) &= -p \nabla \cdot \mathbf{u} - \sum_{m,n=1}^N \nabla \cdot \{ [\nabla \cdot (C_n \mathbf{u})] c_{mn} \nabla C_m \} - \sum_{m=1}^N \nabla \cdot (\mu_m \mathbf{J}_m) + \sum_{m=1}^N \mathbf{J}_m \cdot \nabla \mu_m \\ &\quad + \nabla \cdot \left(\sum_{m,n=1}^N c_{mn} (\nabla C_m \otimes \nabla C_n) \cdot \mathbf{u} \right) - \left(\sum_{m,n=1}^N c_{mn} (\nabla C_m \otimes \nabla C_n) \right) : \nabla \mathbf{u} \\ &\quad - \sum_{m,n=1}^N \nabla \cdot [(\nabla \cdot \mathbf{J}_n) c_{mn} \nabla C_m] - \mathbf{u} \cdot \left[\nabla p_{b,c} - C_3 \nabla \left(\frac{\delta f_{b,c}}{\delta C_3} \right) \right] + \frac{\delta f_{b,c}}{\delta \mathcal{I}} \frac{\partial \mathcal{I}}{\partial t}. \end{aligned} \quad (\text{A20})$$

By substituting Eq. (A20) into Eq. (A12), the latter is reformulated as

$$\begin{aligned} - \frac{d(F_f + E_f)}{dt} + \frac{dW}{dt} &= \int_V \left[\left(p \mathbf{I} + \sum_{m,n=1}^N c_{mn} (\nabla C_m \otimes \nabla C_n) \right) : \nabla \mathbf{u} + \sum_{m=1}^N \nabla \cdot (\mu_m \mathbf{J}_m) - \sum_{m=1}^N \mathbf{J}_m \cdot \nabla \mu_m \right. \\ &\quad + \sum_{m,n=1}^N \nabla \cdot \{ [\nabla \cdot (C_n \mathbf{u})] c_{mn} \nabla C_m \} - \nabla \cdot \left(\sum_{m,n=1}^N c_{mn} (\nabla C_m \otimes \nabla C_n) \cdot \mathbf{u} \right) \\ &\quad + \sum_{m,n=1}^N \nabla \cdot [(\nabla \cdot \mathbf{J}_n) c_{mn} \nabla C_m] + \mathbf{u} \cdot \left[\nabla p_{b,c} - C_3 \nabla \left(\frac{\delta f_{b,c}}{\delta C_3} \right) \right] - \frac{\delta f_{b,c}}{\delta \mathcal{I}} \frac{\partial \mathcal{I}}{\partial t} - \boldsymbol{\sigma}^T : \nabla \mathbf{u} \\ &\quad \left. + \frac{1}{2} \sum_{m=1}^N M_{w,m} \nabla \cdot [(\mathbf{u} \cdot \mathbf{u}) \mathbf{J}_m] - \mathbf{u} \cdot \left(\rho \frac{d\mathbf{u}}{dt} + \sum_{m=1}^N M_{w,m} \mathbf{J}_m \cdot \nabla \mathbf{u} + \nabla \cdot \boldsymbol{\sigma} \right) \right] dV, \end{aligned} \quad (\text{A21})$$

where \mathbf{I} is the second-order identity tensor.

3. Free and kinetic energies of the elastic membrane

Let us focus now on the terms of Eq. (A4) related to the membrane. The free energy F_m of the membrane is the sum of two contributions: strain energy \mathcal{E}_s and bending energy \mathcal{E}_b ,

$$F_m = \mathcal{E}_s + \mathcal{E}_b. \quad (\text{A22})$$

The kinetic energy E_m of the membrane is given by

$$E_m = \frac{1}{2} \int_S m \left| \frac{d\mathbf{X}}{dt} \right|^2 ds, \quad (\text{A23})$$

where the integration takes place over the surface S of the elastic membrane, whose position in Eulerian coordinates at time t is described by $\mathbf{X} = \mathbf{X}(s, t)$, where s denotes its Lagrangian coordinates, and m is the mass surface density of the membrane.

4. Equations of motion

By combining Eqs. (A21)–(A23), the entropy (A4) can be rewritten as

$$\begin{aligned} T \frac{dS}{dt} &= -\frac{d(F_f + E_f)}{dt} - \frac{d(F_m + E_m)}{dt} + \frac{dW}{dt} \\ &= -\int_V \left(\boldsymbol{\sigma}^T - p\mathbf{I} - \sum_{m,n=1}^N c_{mn} (\nabla C_m \otimes \nabla C_n) \right) : \nabla \mathbf{u} dV - \int_V \sum_{m=1}^N \mathbf{J}_m \cdot \nabla \mu_m dV - \int_V \mathbf{u} \cdot \left[\rho \frac{d\mathbf{u}}{dt} + \sum_{m=1}^N M_{w,m} \mathbf{J}_m \cdot \nabla \mathbf{u} \right. \\ &\quad \left. + \nabla \cdot \boldsymbol{\sigma} - \nabla p_{b,c} + C_3 \nabla \left(\frac{\delta f_{b,c}}{\delta C_3} \right) \right] dV - \int_V \frac{\delta f_{b,c}}{\delta \mathcal{I}} \frac{\partial \mathcal{I}}{\partial t} dV - \frac{d\mathcal{E}_s}{dt} - \frac{d\mathcal{E}_b}{dt} - \int_S m \frac{d\mathbf{X}}{dt} \frac{d^2 \mathbf{X}}{dt^2} ds. \end{aligned} \quad (\text{A24})$$

Equation (A24) differs from the expression of the rate of change of the total entropy S in [52] in all but the first terms on the last line, which are present here due to the existence of elastic membranes. We consider the same natural boundary conditions and formulation of the stress tensor $\boldsymbol{\sigma}$ of the ternary fluid as in [52].

According to the second law of thermodynamics, the total entropy cannot decrease over time. This, in combination with the non-negative nature of the third term on the right-hand side of Eq. (A24), implies that

$$\begin{aligned} \rho \frac{d\mathbf{u}}{dt} + \sum_{m=1}^N M_{w,m} \mathbf{J}_m \cdot \nabla \mathbf{u} + \nabla \cdot \boldsymbol{\sigma} - \nabla p_{b,c} \\ + C_3 \nabla \left(\frac{\delta f_{b,c}}{\delta C_3} \right) = 0. \end{aligned} \quad (\text{A25})$$

In this work, we consider that the component weights $M_{w,m}$ are equal, and $\sum_{m=1}^N M_{w,m} \mathbf{J}_m = 0$. For consistency purposes, the ideal gas pressure term p_i in the Navier-Stokes equation

(A25) is separated in the following. As such, the continuity equation (A9) and the Navier-Stokes equation (A25) take, respectively, the form [Eqs. (11) and (12) in Sec. IIC of the article]

$$\frac{\partial \rho}{\partial t} + \nabla \cdot (\rho \mathbf{u}) = 0, \quad (\text{A26})$$

$$\begin{aligned} \frac{\partial (\rho \mathbf{u})}{\partial t} + \nabla \cdot (\rho \mathbf{u} \otimes \mathbf{u}) = -\nabla p_i + \nabla \cdot [\eta (\nabla \mathbf{u} + \nabla \mathbf{u}^T)] \\ - \rho \nabla \mu_\rho - \phi \nabla \mu_\phi - \psi \nabla \mu_\psi \\ - \psi \nabla \left(\frac{\delta f_{b,c}}{\delta \psi} \right), \end{aligned} \quad (\text{A27})$$

where the auxiliary fields $\phi = C_1 - C_2$ and $\psi = C_3$ [Eq. (10) in Sec. IIC of the article] have also been introduced. The equation of motion of the elastic membrane can be derived by considering the last four terms on the right-hand side of Eq. (A24), and setting their sum equal to zero.

-
- [1] M. Scott Long, C. D. Jones, M. R. Helfrich, L. K. Mangeney-Slavin, and C. D. Keating, *Proc. Natl. Acad. Sci. USA* **102**, 5920 (2005).
- [2] Y. Li, H. Kusumaatmaja, R. Lipowsky, and R. Dimova, *J. Phys. Chem. B* **116**, 1819 (2012).
- [3] H. N. Yow and A. F. Routh, *Soft Matter* **2**, 940 (2006).
- [4] L. J. De Cock, S. De Koker, B. G. De Geest, J. Grooten, C. Vervaet, J. P. Remon, G. B. Sukhorukov, and M. N. Antipina, *Angew. Chem. Int. Ed.* **49**, 6954 (2010).
- [5] I. M. Martins, M. F. Barreiro, M. Coelho, and A. E. Rodrigues, *Chem. Eng. J.* **245**, 191 (2014).
- [6] A. Gharsallaoui, G. Roudaut, O. Chambin, A. Voilley, and R. Saurel, *Food Res. Int.* **40**, 1107 (2007).
- [7] S. C. Glotzer and M. J. Solomon, *Nat. Mater.* **6**, 557 (2007).
- [8] A. B. Pawar and I. Kretzschmar, *Macromol. Rapid Commun.* **31**, 150 (2010).
- [9] C.-M. Lo, H.-B. Wang, M. Dembo, and Y.-L. Wang, *Biophys. J.* **79**, 144 (2000).
- [10] D. E. Discher, P. Janmey, and Y.-L. Wang, *Science* **310**, 1139 (2005).
- [11] X. Yao, Y. Hu, A. Grinthal, T.-S. Wong, L. Mahadevan, and J. Aizenberg, *Nat. Mater.* **12**, 529 (2013).

- [12] J. Bico, B. Roman, L. Moulin, and A. Boudaoud, *Nature (London)* **432**, 690 (2004).
- [13] I. L. Ivanovska, P. J. de Pablo, B. Ibarra, G. Sgalari, F. C. MacKintosh, J. L. Carrascosa, C. F. Schmidt, and G. J. L. Wuite, *Proc. Natl. Acad. Sci. USA* **101**, 7600 (2004).
- [14] M. Buenemann and P. Lenz, *Phys. Rev. E* **78**, 051924 (2008).
- [15] J. Hegemann, H.-H. Boltz, and J. Kierfeld, *Soft Matter* **14**, 5665 (2018).
- [16] M. Scott Long, A.-S. Cans, and C. D. Keating, *J. Am. Chem. Soc.* **130**, 756 (2008).
- [17] H. Kusumaatmaja, Y. Li, R. Dimova, and R. Lipowsky, *Phys. Rev. Lett.* **103**, 238103 (2009).
- [18] H. Kusumaatmaja and R. Lipowsky, *Soft Matter* **7**, 6914 (2011).
- [19] V. Meester, R. W. Verweij, C. van der Wel, and D. J. Kraft, *ACS Nano* **10**, 4322 (2016).
- [20] A. Marchand, S. Das, J. H. Snoeijer, and B. Andreotti, *Phys. Rev. Lett.* **109**, 236101 (2012).
- [21] R. W. Style and E. R. Dufresne, *Soft Matter* **8**, 7177 (2012).
- [22] R. W. Style, Y. Che, S. J. Park, B. M. Weon, J. H. Je, C. Hyland, G. K. German, M. P. Power, L. A. Wilen, J. S. Wettlaufer, and E. R. Dufresne, *Proc. Natl. Acad. Sci. USA* **110**, 12541 (2013).
- [23] J. Bico, É. Reyssat, and B. Roman, *Annu. Rev. Fluid Mech.* **50**, 629 (2018).
- [24] C. Duprat, J. M. Aristoff, and H. A. Stone, *J. Fluid Mech.* **679**, 641 (2011).
- [25] K. Singh, J. R. Lister, and D. Vella, *J. Fluid Mech.* **745**, 621 (2014).
- [26] A. Sauret, F. Boulogne, D. Cébron, E. Dressaire, and H. A. Stone, *Soft Matter* **11**, 4034 (2015).
- [27] S. Ramanujan and C. Pozrikidis, *J. Fluid Mech.* **361**, 117 (1998).
- [28] J. Zhang, P. C. Johnson, and A. S. Popel, *Phys. Biol.* **4**, 285 (2007).
- [29] S. K. Doddi and P. Bagchi, *Int. J. Multiphase Flow* **34**, 375 (2008).
- [30] S. K. Doddi and P. Bagchi, *Int. J. Multiphase Flow* **34**, 966 (2008).
- [31] E. Foessel, J. Walter, A.-V. Salsac, and D. Barthès-Biesel, *J. Fluid Mech.* **672**, 477 (2011).
- [32] Z. Y. Luo and B. F. Bai, *Phys. Fluids* **28**, 101901 (2016).
- [33] Z. Y. Luo and B. F. Bai, *J. Fluid Mech.* **840**, 656 (2018).
- [34] B. Kaoui, G. H. Ristow, I. Cantat, C. Misbah, and W. Zimmermann, *Phys. Rev. E* **77**, 021903 (2008).
- [35] D. Barthès-Biesel, *Annu. Rev. Fluid Mech.* **48**, 25 (2016).
- [36] L. A. Lubbers, J. H. Weijers, L. Botto, S. Das, B. Andreotti, and J. H. Snoeijer, *J. Fluid Mech.* **747**, R1 (2014).
- [37] J. Bueno, H. Casquero, Y. Bazilevs, and H. Gomez, *Meccanica* **53**, 1221 (2018).
- [38] M. Wouters, O. Aouane, T. Krüger, and J. Harting, *Phys. Rev. E* **100**, 033309 (2019).
- [39] M. R. Swift, W. R. Osborn, and J. M. Yeomans, *Phys. Rev. Lett.* **75**, 830 (1995).
- [40] M. R. Swift, E. Orlandini, W. R. Osborn, and J. M. Yeomans, *Phys. Rev. E* **54**, 5041 (1996).
- [41] A. J. Briant, A. J. Wagner, and J. M. Yeomans, *Phys. Rev. E* **69**, 031602 (2004).
- [42] A. J. Briant and J. M. Yeomans, *Phys. Rev. E* **69**, 031603 (2004).
- [43] T. Lee and C.-L. Lin, *J. Comput. Phys.* **206**, 16 (2005).
- [44] A. Mazloomi M., S. S. Chikatamarla, and I. V. Karlin, *Phys. Rev. Lett.* **114**, 174502 (2015).
- [45] C. Semprebbon, T. Krüger, and H. Kusumaatmaja, *Phys. Rev. E* **93**, 033305 (2016).
- [46] M. Wöhrwag, C. Semprebbon, A. Mazloomi Moqaddam, I. Karlin, and H. Kusumaatmaja, *Phys. Rev. Lett.* **120**, 234501 (2018).
- [47] X. Shan and H. Chen, *Phys. Rev. E* **47**, 1815 (1993).
- [48] L. Chen, Q. Kang, Y. Mu, Y.-L. He, and W.-Q. Tao, *Int. J. Heat Mass Transfer* **76**, 210 (2014).
- [49] T. Krüger, H. Kusumaatmaja, A. Kuzmin, O. Shardt, G. Silva, and E. M. Vigen, *The Lattice Boltzmann Method—Principles and Practice* (Springer, Switzerland, 2017).
- [50] C. S. Peskin, *J. Comput. Phys.* **25**, 220 (1977).
- [51] K. A. Brakke, *Exp. Math.* **1**, 141 (1992).
- [52] J. Kou and S. Sun, *Comput. Methods Appl. Mech. Eng.* **331**, 623 (2018).
- [53] T. Krüger, F. Varnik, and D. Raabe, *Comput. Math. Appl.* **61**, 3485 (2011).
- [54] P. L. Bhatnagar, E. P. Gross, and M. Krook, *Phys. Rev.* **94**, 511 (1954).
- [55] A. L. Kupershtokh, Proceedings of the 5th International EHD Workshop, University of Poitiers, Poitiers, France (2004), p. 241.
- [56] C. S. Peskin, *Acta Numer.* **11**, 479 (2002).
- [57] F. Sotiropoulos and X. Yang, *Prog. Aerosp. Sci.* **65**, 1 (2014).
- [58] W. Kim and H. Choi, *Int. J. Heat Fluid Flow* **75**, 301 (2019).
- [59] B. A. Grzybowski, N. Bowden, F. Arias, H. Yang, and G. M. Whitesides, *J. Phys. Chem. B* **105**, 404 (2001).
- [60] S. H. Collicott and M. M. Weislogel, *AIAA J.* **42**, 289 (2004).
- [61] C. Semprebbon, M. Scheel, S. Herminghaus, R. Seemann, and M. Brinkmann, *Phys. Rev. E* **94**, 012907 (2016).
- [62] O. V. Manyuhina, J. J. Hetzel, M. I. Katsnelson, and A. Fasolino, *Eur. Phys. J. E* **32**, 223 (2010).